remote sensing

MDPI

Article

Deformation Characteristics and Activation Dynamics of the Xiaomojiu Landslide in the Upper Jinsha River Basin Revealed by Multi-Track InSAR Analysis

Xu Ma [1], Junhuan Peng [1,*], Yuhan Su [1], Mengyao Shi [2], Yueze Zheng [1,3], Xu Li [1] and Xinwei Jiang [1]

[1] School of Land Science and Technology, China University of Geosciences, Beijing 100083, China; maxu@email.cugb.edu.cn (X.M.); s_yuhan@163.com (Y.S.); zheng_cugb@163.com (Y.Z.); lixu2021@163.com (X.L.); gzhzy1996@163.com (X.J.)
[2] Faculty of Land Resources Engineering, Kunming University of Science and Technology, Kunming 650093, China; shimengyao@kust.edu.cn
[3] Beijing Institute of Surveying and Mapping, Beijing 100038, China
* Correspondence: pengjunhuan@163.com

Abstract: The upper Jinsha River, located in a high-mountain gorge with complex geological features, is highly prone to large-scale landslides, which could result in the formation of dammed lakes. Analyzing the movement characteristics of the typical Xiaomojiu landslide in this area contributes to a better understanding of the dynamics of landslides in the region, which is of great significance for landslide risk prediction and analysis. True displacement data on the surface of landslides are crucial for understanding the morphological changes in landslides, providing fundamental parameters for dynamic analysis and risk assessment. This study proposes a method for calculating the actual deformation of landslide bodies based on multi-track Interferometric Synthetic Aperture Radar (InSAR) deformation data. It iteratively solves for the optimal true deformation vector of the landslide on a per-pixel basis under a least-squares constraint based on the assumption of consistent displacement direction among adjacent points on the landslide surface. Using multi-track Sentinel data from 2017 to 2023, the line of sight (LOS) accumulative de-formation of the Xiaomojiu landslide was obtained, with a maximum LOS deformation of −126 mm/year. The true surface displacement of the Xiaomojiu landslide after activation was calculated using LOS deformation. The development of two rotational sub-slipping zones on the landslide body is inferred based on the distribution of actual displacements along the central profile line. Analysis of temporal changes in water body area data revealed that the Xiaomojiu landslide was activated after a barrier lake event and continuously moved due to the influence of higher water levels' in the river channel. In conclusion, the proposed method can be applied to calculate the true surface displacement of landslides with complex mechanisms for analyzing the movement status of landslide bodies. Furthermore, the spatiotemporal analysis of the Xiaomojiu landslide characteristics can support analyzing the mechanisms of similar landslides in the Jinsha River Basin.

Keywords: Sentinel-1; Xiaomojiu landslide; 3D displacements; SBAS-InSAR; Multi-Track InSAR

Citation: Ma, X.; Peng, J.; Su, Y.; Shi, M.; Zheng, Y.; Li, X.; Jiang, X. Deformation Characteristics and Activation Dynamics of the Xiaomojiu Landslide in the Upper Jinsha River Basin Revealed by Multi-Track InSAR Analysis. *Remote Sens.* **2024**, *16*, 1940. https://doi.org/10.3390/rs16111940

Academic Editor: Alex Hay-Man Ng

Received: 16 April 2024
Revised: 20 May 2024
Accepted: 21 May 2024
Published: 28 May 2024

1. Introduction

Landslides, a common geological hazard worldwide, cause billions of dollars in losses and thousands of casualties annually [1,2]. The frequency of landslides has been increasing annually due to human engineering activities and the increase in extreme rainfall caused by global climate change [3]. In the Qinghai–Tibet Plateau region of China, where geological conditions are complex, the significant uplift of the plateau crust and the rapid incision of rivers have led to widespread instability on both sides of river valleys [4,5]. The Jinsha River valley's steep terrain and narrow channels make it prone to landslides that can easily block the river, forming barrier lakes [6]. In 2018, the Baige landslide, a high-altitude,

long-range event, occurred in the area, blocking the main channel of the upper reaches of the Jinsha River and creating a barrier lake [7,8]. Consequently, the breach of the barrier lake dam led to a flood disaster, resulting in a direct economic loss of USD 960 million [9,10]. Moreover, the abrupt fluctuations in the river channel's water level following the dam break stimulated the reactivation of the Xiaomojiu ancient landslide situated 5 km upstream [11]. Therefore, continuous monitoring of the Xiaomojiu landslide is crucial to prevent similar disasters [12].

In landslide-prone areas, various remote sensing technologies are currently being utilized for comprehensive surface deformation monitoring [13–16]. Among these technologies, InSAR is widely used due to its broad coverage and high accuracy [17,18]. For instance, InSAR technology has been utilized to capture the pre-failure deformation of the Baige landslide, confirming the adherence of the landslide deformation history to the three-stage creep theory [19]. Particularly during the initial phase of landslide deformation, InSAR technology can track the surface displacement of the landslide mass, which, in turn, facilitates the deduction of geometric characteristics of the landslide surface [20]. These results help analyze the structure of landslides and serve as an essential technical tool for assisting landslide motion analysis.

InSAR technology has proven to be a valuable tool for monitoring surface deformation; however, it is not without limitations. In particular, the polar orbit side-looking mode of InSAR satellites means that a single synthetic aperture radar SAR platform typically only captures one-dimensional deformation along the radar line of sight (LOS) [21]. This limitation is compounded by topographic shadowing, vegetation coverage, and surface deformation gradients, which can significantly impact monitoring results. The challenge arises when the LOS displacement, which is the projection of the surface displacement vector onto the LOS, is perpendicular to the surface displacement [22], making it challenging to detect surface deformation accurately. To overcome the limitations of InSAR technology and capture a broader range of surface deformation scenarios, obtaining measurements in three different directions or having equivalent prior information is essential [23]. By restoring the true surface deformation through multiple measurements, researchers can enhance the accuracy and reliability of InSAR monitoring results.

In estimating true three-dimensional deformation from one-dimensional observations, the rank deficiency caused by insufficient observations can be improved by imposing additional constraints or including unrelated observations. Therefore, landslide deformation inversion based on InSAR technology can be categorized into two main approaches. The first method involves increasing constraints by incorporating true observations, which can be further categorized into homogeneous and heterogeneous subclasses. In the homogeneous subclass, it is defined as utilizing Spaceborne SAR data to obtain horizontal deformation in the north-south direction through alternative processing methods [23] (e.g., Pixel Offset Tracking (POT) [24], Multi-Aperture Interferometry (MAI) [25], and various combinations of satellite observations). However, the accuracy of POT technology is influenced by data spatial resolution. In contrast, MAI technology is constrained by coherence, resulting in lower accuracy than LOS deformation obtained through time-series InSAR. In the heterogeneous subclass utilizing non-spaceborne SAR data, such as Global Navigation Satellite Systems (GNSS) [26], unmanned aerial vehicles [27], and ground-based SAR [28,29]. Nonetheless, obtaining diverse multi-source observational data is often challenging due to factors like the spatial distribution of landslides and data acquisition costs.

The second method, which involves adding constraints through prior information to reduce the required true observations [30], has become a standard technique for landslide deformation inversion. For example, in east-west landslides, the north-south horizontal deformation is often neglected [20], or models like the Surface Parallel Flow Model (SPFM) are used [31–33]. SPFM is frequently applied to translational landslides [34] but is unsuitable for rotational landslides with arcuate sliding surfaces [35,36]. However, assumptions made in advance regarding the sliding direction of the landslide mass may significantly differ from the true complex movements of the landslide. Therefore, in some studies [37],

based on the local parallel flow assumption, landslides are assumed to be composed of multiple landslide sub-blocks, where each sub-block shares a uniform sliding surface motion direction. The partitioning of landslide sub-blocks plays a significant role in the reliability of this approach's deformation inversion.

Therefore, this study does not initially divide landslide blocks but infers the real 3D (three-dimensional) displacements on the landslide surface by assuming that adjacent points on the surface are in the same direction. We apply this approach to the Xiaomojiu landslide in the Jinsha River Basin. The true motion displacements and directions on the landslide surface were inferred using multi-track Sentinel data. Compared to conventional methods, this approach does not require prior knowledge of the landslide block boundaries and better reproduces the true motion characteristics of the landslide body. The method calculates the actual deformation of landslides, which can be used to analyze the spatiotemporal attributes of other landslides in the area. Additionally, calculating the actual landslide deformation can help deduce the sliding surface and thickness of the landslide body during the slow deformation stages [31,38,39], providing data support for assessing the extent of damage caused by landslide failure in subsequent simulations. Based on the actual deformation results and water area data, this study discusses the spatiotemporal variations and driving factors of the Xiaomojiu landslide.

2. Study Area

The Jinsha River Basin, situated in the eastern part of the Qinghai-Tibet Plateau, is characterized by intense crustal movement and frequent seismic activity [40]. This basin exhibits complex geological and geomorphological conditions, forming numerous large-scale, deep-seated creeping landslides [41]. One such significant landslide, the Xiaomojiu landslide, is situated in the V-shaped valley of the upper Jinsha River. The main steep slope of this landslide has a peak elevation of approximately 3655 m, while the toe of the landslide sits at around 2895 m, resulting in a relative height difference of 760 m between the two points. The overall slope inclination ranges between 30~35° (Figure 1). Due to lateral erosion from the Jinsha River, the landslide is typical of a high-steep valley-shaped fragmented loose body [42]. The geological lithology in the area mainly comprises metamorphic ultramafic rocks (including chlorite schist and serpentinite), metamorphic clastic rocks (such as quartz-sericite schist, biotite-muscovite quartz schist, hornfels, and slate), as well as marble [43]. The structural context of the region is primarily influenced by the Jinsha River fault zone, with the main fault trending NW-SE located approximately 1 km from the Xiaomojiu landslide. The presence of this fault significantly impacts the development of the landslide [11,44]. Historical records document destructive events associated with this landslide [45]. Previous exploration studies have revealed that the primary components of the landslide body consist of gravel and clay, with no bedrock detected even at a drilling depth of 60 m, highlighting the thick accumulation characteristics of the landslide body [42].

The Baige landslide event had a significant impact on the water level in the region. Before the Baige landslide, the average elevation of the riverbed in that section was 2870 m. However, after the secondary dam breach, the elevation at the bottom of the spillway rose to 2903 m [46]. This event resulted in an overall increase in the water level upstream of the Baige landslide, significantly affecting the surrounding geological environment. As of 21 April 2023, optical images show that the remaining dam debris still blocks the Jinsha River channel (Figure 1d). The dam breach event directly triggered the activation of the Xiaomojiu landslide [11], leading it into the uniform deformation stage [47]. In the long term, the continued higher water level may have a lasting adverse effect on the stability of the Xiaomojiu landslide mass.

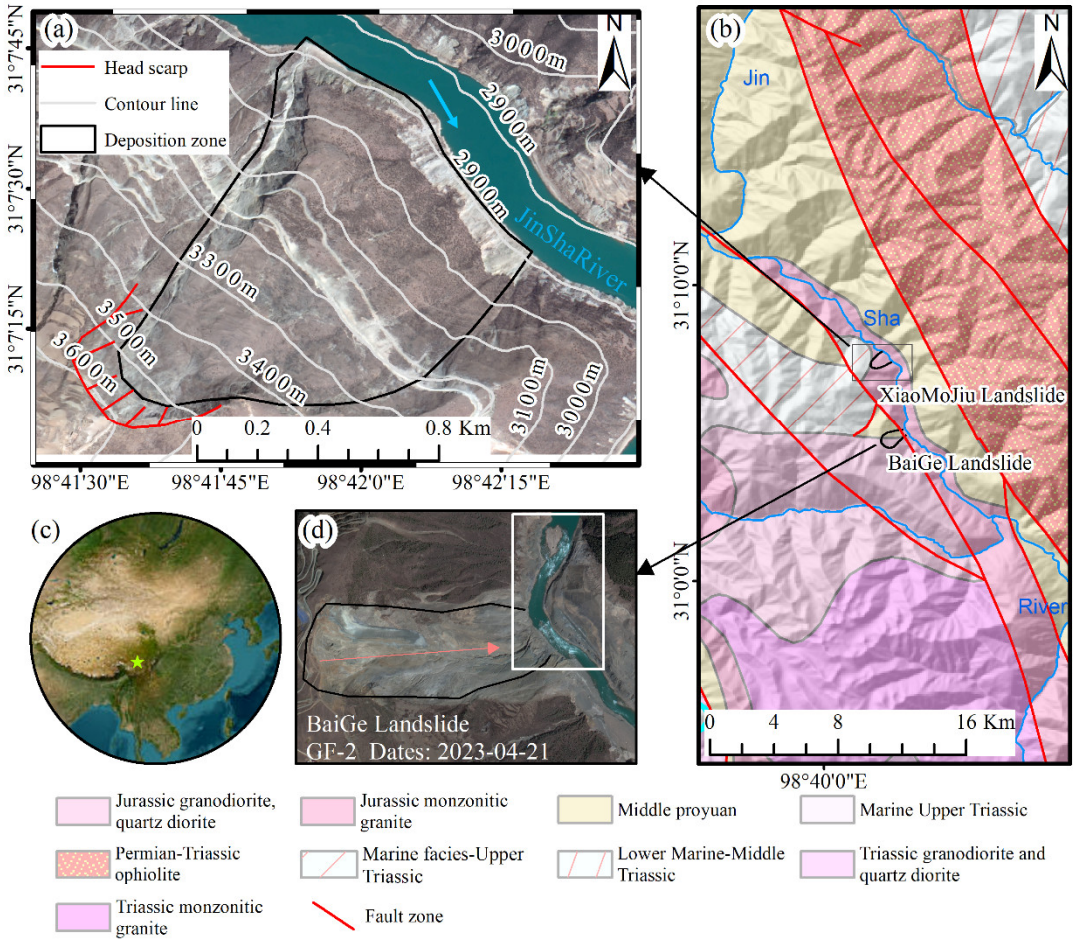

Figure 1. (**a**) Optical image of the Xiaomojiu landslide, (**b**) geological map of the study area at 1:2,500,000 scale, (**c**) map showing the location of the Xiaomojiu landslide, (**d**) schematic image showing the remaining debris blocking the river channel after the breach of the Baige landslide barrier lake.

3. Data and Methods

3.1. Data

This study to obtain the long-term deformation of the Xiaomojiu landslide, collected Sentinel-1A/B images from October 2017 to September 2023, including 139 ascending orbit images from path 99 (A99), 153 descending orbit images from path 33 (D33), and 168 descending orbit images from path 106 (D106). The detailed information on the Sentinel-1 SAR data is shown in Table 1. We sequentially processed the data from each direction to obtain time-series deformation data. The ALOS World 3D-30m (AW3D30) Digital Elevation Model (DEM) was obtained from the JAXA Earth Observation Research Center [48], and precise orbit determination (POD) products were acquired from the Copernicus Sentinels POD Data Hub. Additionally, monthly total precipitation data from 2017 to 2022, with a spatial resolution of 1 km, were obtained from the Institute of Tibetan Plateau Research, Chinese Academy of Sciences [49]. Optical image data from GF-2 and GF-7 were obtained from the China Aero Geophysical Survey and Remote Sensing Center for Land and Resources (AGRS).

Table 1. Detailed information on Sentinel-1 data.

Period	Orbit	Incidence Angle (°)	Heading Angle (°)	Path	Frame	Number of Scenes
8 October 2017~ 19 September 2023	Ascending	35.76	347.22	99	1280	139
15 October 2017~ 20 October 2023	Descending	43.92	192.77	33	487	153
8 October 2017~ 7 September 2023	Descending	31.92	192.80	106	486	168

3.2. Methods

This section focuses on the operations performed to obtain the true displacement of the landslide surface. We can split the proposed approach into two processing steps: First, SBAS-InSAR obtains three LOS cumulative deformations. Second, adjacent orientation consistency is used to invert the landslide to true displacement. The workflow diagram illustrating the InSAR data processing, and the method proposed in this paper is detailed in Figure 2.

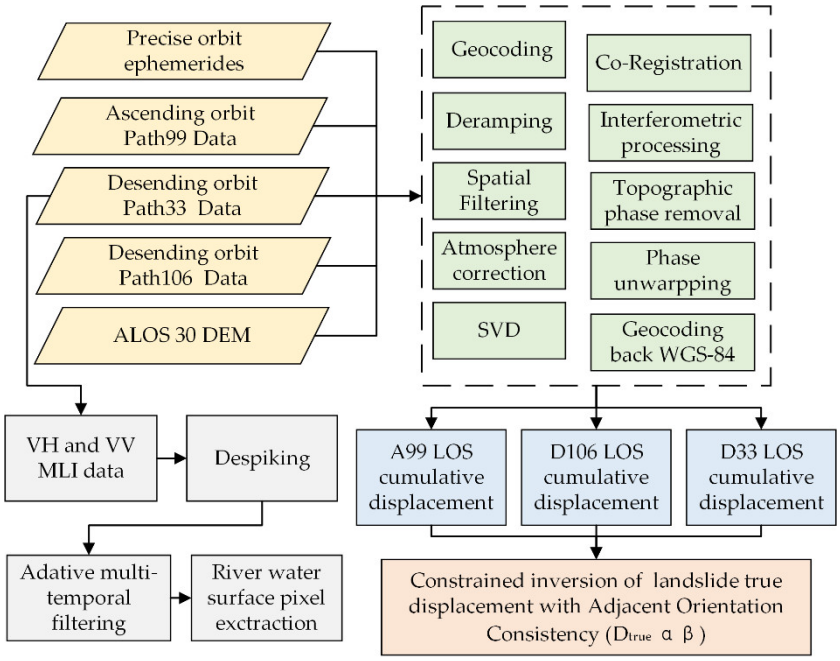

Figure 2. Flowchart for the SAR data processing and true deformation inversion.

3.2.1. InSAR Processing

This study employs the Small Baseline Subset InSAR (SBAS-InSAR) [50] processing method to obtain a long-term displacement time series of surface movement in the landslide area along three orbital LOS directions. Firstly, the ascending and descending images covering the study area are individually geocoded and registered. Subsequently, the registered data are geocoded, and corresponding mask files are generated to remove geometric distortions and shadow regions. A multi-look ratio of 4 (range) and 1 (azimuth) was employed on SAR images to enhance the signal-to-noise ratio and image consistency while balancing the density of landslide monitoring points. This ratio was chosen to match the spatial resolution of the imagery, with DEM resolution interpolated to the same level. Next, differential interferograms are generated from the registered images, with the temporal and spatial baselines of interferograms illustrated in Figure 3. A Goldstein filter with a window size of 32 × 32 pixels is applied to the interferogram to remove the topographic and flat-earth phase components to enhance the signal-to-noise ratio. The phase unwrap-

ping is then performed using the Minimum Cost Flow algorithm (MCF) [51]. At this stage, we can examine the primary components of the unwrapped phase interferograms in detail in Equation (1). Linear regression is applied to remove the terrain residual phase components φ_{res} from the unwrapped phase. Using empirical linear elevation models and spatiotemporal filtering eliminates atmospheric phase components φ_{atm} [52]. Finally, the deformation phase components φ_{disp} are estimated using Singular Value Decomposition (SVD), cumulative deformation is calculated, and the results are re-encoded into the WGS84 coordinate system for further assessment of landslide 3D movement.

$$\varphi_{unw} = \varphi_{res} + \varphi_{atm} + \varphi_{disp} + \varphi_{noise} \quad (1)$$

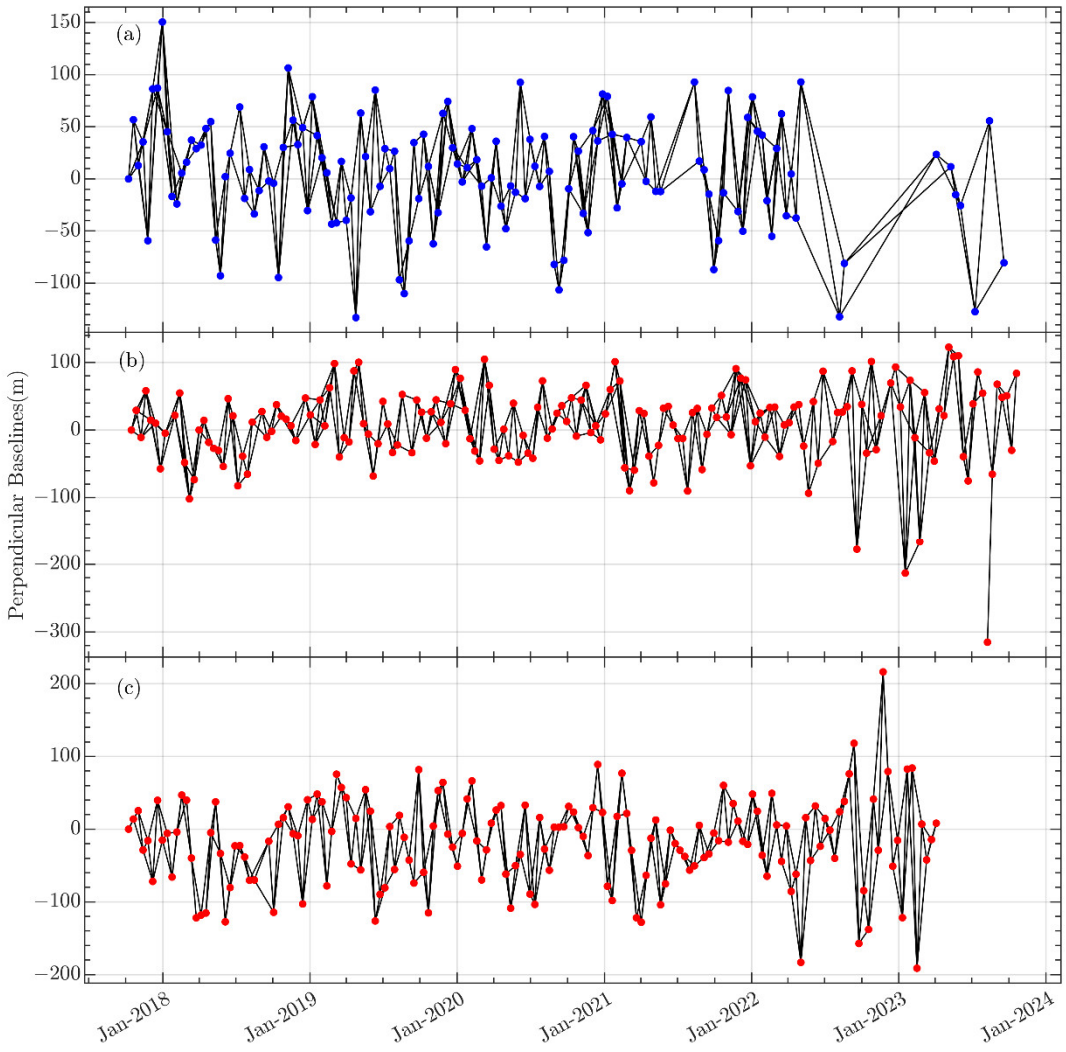

Figure 3. This study used the spatial and temporal baselines of the Sentinel-1 data from Ascending orbit Path 99 (**a**), Descending orbit Path 33 (**b**), and Descending orbit Path 106 (**c**). Blue dots represent ascending track data, and red dots represent descending track data.

3.2.2. Landslide True Ground Displacement and LOS Conversion Coefficients

The LOS deformation obtained from time-series InSAR represents the projection of true surface displacement in that direction, as depicted in Figure 4. Unit vectors of LOS direction in the north, earth, and up (NEU) directions $[\sin\theta\sin\varphi \quad -\sin\theta\cos\varphi \quad \cos\theta]^T$ represent the satellite's incidence angle and denote the satellite's azimuth angle. The unit vectors of true ground deformation in the NEU directions can be represented as $[\cos\alpha\cos\beta \quad \cos\alpha\sin\beta \quad \sin\alpha]^T$, where α is the angle between the true displacement vector

and the horizontal plane $\alpha \in [-\pi/2, \pi/2]$ and $\alpha < 0$ when the vertical component of the true deformation vector is downward. The β represent the azimuth angles of the true displacement vector [53].

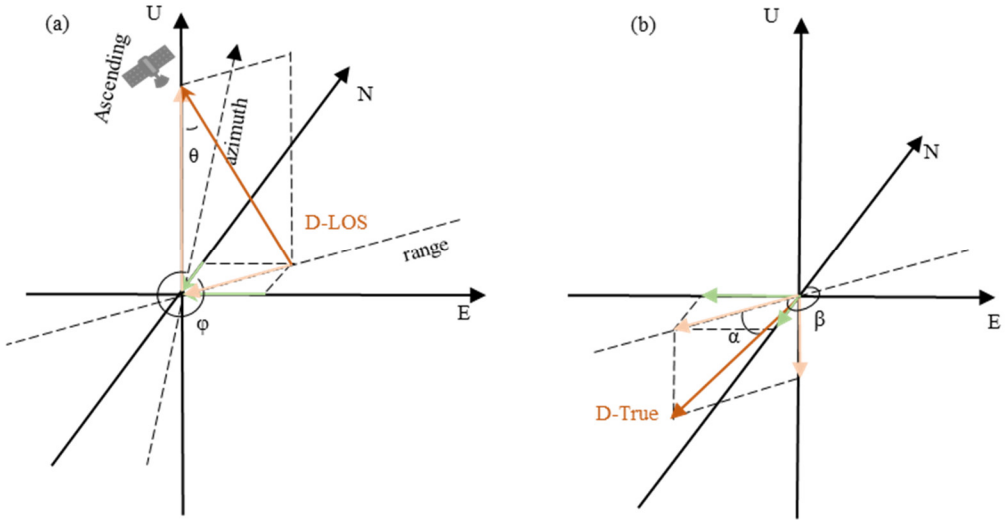

Figure 4. (**a**) NEU-directional projection delineates the satellite LOS motion vector. (**b**) NEU-directional projection of the authentic ground deformation vector.

The geometric transformation relationship between the observed LOS displacement L_{los} and the true surface deformation D_{true} can be expressed by the Equation (2).

$$L_{los} + \Delta l = \mathrm{C} \cdot D_{true} \tag{2}$$

where L_{los} takes negative values when far from the satellite and positive values when close to the satellite; Δl represents the observation error, and C represents the projection coefficient of the LOS observation direction onto the unit vector of the true deformation direction [53]. Its calculation formula is shown in the Equation (3).

$$\begin{aligned} C &= \sin\theta \sin\varphi \cdot \cos\alpha \cos\beta - \sin\theta \cos\varphi \cdot \cos\alpha \sin\beta + \cos\theta \cdot \sin\alpha \\ &= \sin\theta \cdot \cos\alpha \cdot \sin(\varphi - \beta) + \cos\theta \cdot \sin\alpha \end{aligned} \tag{3}$$

The true surface displacement vector consists of D_{true}, α, and β, representing the magnitude and direction of the true displacement vector. When the assumption of surface parallel flow is employed, $\alpha = -\angle Slope$, $\beta = \angle Aspect$. In this case, the conversion coefficients are called C-index [54–56], commonly used to evaluate the sensitivity of detecting landslide deformations in the LOS direction or to assist in landslide identification [2,55]. The C-index is equivalent to the projection coefficient of surface deformation in the LOS direction for translational landslides, where the movement direction aligns with the slope gradient.

To preliminarily analyze the movement characteristics of the Xiaomojiu landslide, we computed the C-index results for the Xiaomojiu landslide area on three orbits based on the slope and aspect derived from the AW3D DEM (see Figure 5), following Equation (3). The C-index distribution reveals that, under the assumption of surface parallel flow, the sensitivity to deformations associated with movement along the slope gradient is in the order of A99 > D33 > D106. Specifically, deformations projected onto A99 are predominantly negative, while those on the descending orbits D33 and D106 are primarily positive. Due to differences in the incidence angles, the absolute values of the C-index on the D106 orbit are smaller than those on the D33 orbit. Under the assumption of surface parallel flow, the distribution of positive and negative LOS deformations theoretically aligns with the C-index distribution when the landslide body moves along the slope gradient.

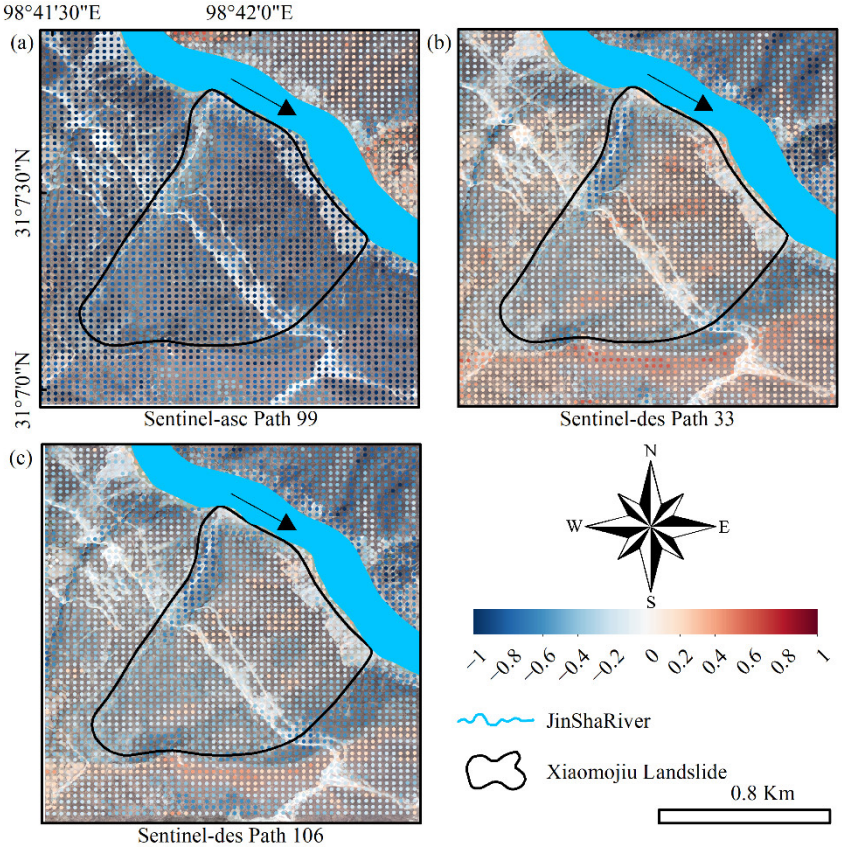

Figure 5. C-index distribution for the Xiaomojiu landslide on three orbits: (**a**) orbit A99, (**b**) orbit D33, and (**c**) orbit D106. The black arrow represents the direction of the river flow. Positive values indicate proximity to the satellite, while negative values indicate distance from the satellite. When $|C| = 1$, the LOS direction is parallel to the direction of the steepest slope, and when $C = 0$, the LOS direction is perpendicular to the direction of the steepest slope.

In cases of non-translational landslide movement, the C-index may fail to accurately reflect the relationship between the actual deformation of the landslide and the LOS deformation. For a point on the landslide body, the observations in different LOS directions represent the projection of the true deformation vector onto those LOS directions. The detectability and sensitivity of landslide deformation measurements are determined by factors such as the ground deformation gradient, InSAR imaging geometry, and coherence [57]. When the landslide deformation is not affected by geometric distortions and is detectable, the geometric relationship between the LOS direction determined by InSAR imaging geometry and the true deformation vector is crucial for estimating the true deformation. Therefore, this study computed the projection coefficients of true deformation in arbitrary directions onto the three LOS directions (see Figure 6). The azimuth look direction (ALD) is the clockwise angle between the LOS projection on the horizontal plane and the north direction [58]. Given the possibility of landslide expansion and toe bulging, the deformation of the landslide body may include a vertical component. Thus, two scenarios were considered: corresponding to Figure 6a–c, while corresponding to Figure 6d–f. In observable regions on the ground, when the LOS deformation vector is nearly perpendicular to the actual deformation vector, the projection of actual deformation onto the LOS direction approaches zero, indicating low sensitivity of the LOS direction to the actual deformation at that location. Figure 6 shows that data from different orbits can complement each other, except for horizontal deformations in the north–south direction.

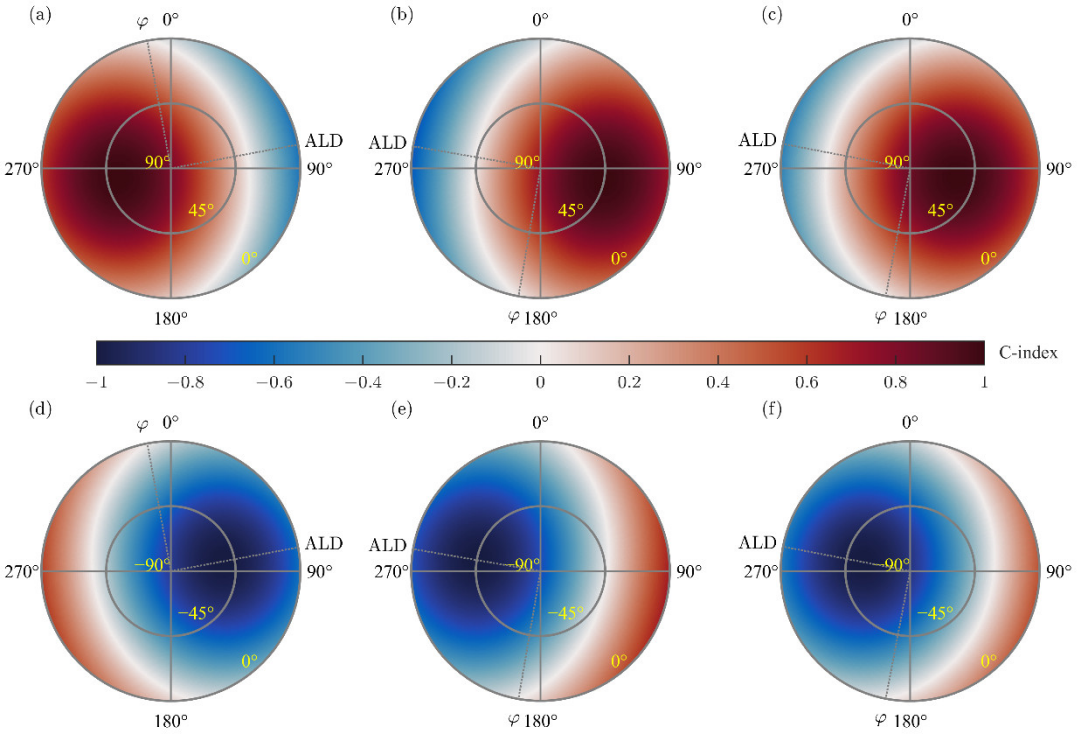

Figure 6. Different combinations of ground displacement directions correspond to projection coefficient C-index values, (**a**,**d**)ascending path 99; (**b**,**e**) descending path 33; (**c**,**f**) descending path 106.

3.2.3. Adjacent Orientation Consistency Constrained Inversion of True Displacement

In addition to determining the direction of true displacement in advance using the SPFM to solve for the true deformation vector, other methods, such as prior information, can be employed to partition the landslide body into regions. This approach assumes that the sliding direction within individual landslide blocks is consistent, enabling the solution of the true deformation direction within each landslide sub-block by combining observations from different directions [37,59]. Alternatively, fixed motion directions can be assumed to solve for the true deformation displacement, as demonstrated by models such as the Aspect Parallel Flow Model (APFM) and the Steepest Terrain Following Model (STFM) [60–62]. Considering the similarity in the motion direction of adjacent points in space, this study assumes that the true displacement direction of neighboring points in the landslide space is consistent, facilitating the solution of the true deformation of the landslide body.

Assuming there are m different orbits or types of data observations for n spatially adjacent points within the same sliding unit on the landslide body, it can be assumed that they share a consistent displacement direction $\begin{bmatrix}\alpha & \beta\end{bmatrix}^T$. However, given that the true displacement $\begin{bmatrix}x_1 & x_2 & \cdots & x_n\end{bmatrix}^T$ of the n points may vary, a total of $m{\cdot}n$ observation equations can be constructed. For the jth point in the ith orbit observation, the projection of the true deformation in its observation direction can be represented by the following nonlinear function:

$$\begin{gathered}\widetilde{L}_k = [\sin\theta_i \cdot \cos\alpha \cdot \sin(\varphi_i - \beta) + \cos\theta_i \cdot \sin\alpha] \cdot x_j \\ i \in [1, m], j \in [1, n]\end{gathered} \tag{4}$$

where $\widetilde{L}_k$ represents the corresponding function for this observation and $k = (i-1)n + j$ denotes the observation sequence number in the observation equation set. Letting $f_k(\alpha, \beta, x_j) =$

$[\sin\theta_i \cdot \cos\alpha \cdot \sin(\varphi_i - \beta) + \cos\theta_i \cdot \sin\alpha] \cdot x_j$, a system of the following nonlinear equations can be constructed for all points in the point set.

$$\begin{aligned} \underset{mn\times 1}{\mathbf{F}}(\mathbf{X}) &= \begin{bmatrix} f_1 & f_2 & \cdots & f_k & \cdots & f_{mn} \end{bmatrix}^T \\ \underset{n+2}{\mathbf{X}} &= \begin{bmatrix} \alpha & \beta & x_1 & x_2 & \cdots & x_n \end{bmatrix}^T \end{aligned} \tag{5}$$

Based on the equation set above, the observation function can be constructed, and the specific form of the error model is as follows:

$$\begin{aligned} \underset{mn\times 1}{\mathbf{L}} &= \underset{mn\times 1}{\mathbf{F}}(\mathbf{X}) - \underset{mn\times 1}{\mathbf{\Delta}} \\ D_{\mathbf{L}} &= \sigma_0^2 \mathbf{P}^{-1} \end{aligned} \tag{6}$$

where $\underset{mn\times 1}{\mathbf{L}}$ represents the matrix of observed values, $\underset{mn\times 1}{\mathbf{F}}(\mathbf{X})$ is the corresponding matrix of nonlinear functions, and $\underset{mn\times 1}{\mathbf{\Delta}}$ is the error matrix. The angles represent the direction of the true deformation vector α and β are bounded $\alpha \in [\frac{-\pi}{2}, \frac{\pi}{2}]$, $\beta \in [0, 2\pi]$. The true deformation vector can be estimated using nonlinear least squares constrained optimization [63].

$$\hat{\mathbf{X}} = \text{argmin}||G(\bullet)||^2 \tag{7}$$

where the function G represents the loss function, which can be chosen based on the specific circumstances, when employing nonlinear least squares optimization, it is as follows:

$$\begin{aligned} \mathbf{V} &= \mathbf{F}(\hat{\mathbf{X}}) - \mathbf{L} \\ G &= \mathbf{V}^T \mathbf{P} \mathbf{V} \end{aligned} \tag{8}$$

where $\mathbf{V}$ is the error vector, and $\hat{\mathbf{X}}$ represents the estimated values of the true deformation. Based on the above method, the true surface deformation can be calculated according to the LOS deformations obtained from different orbits.

4. Results: Xiaomojiu Landslides Displacement between October 2017 to September 2023

4.1. InSAR LOS Deformation Results

Based on the Sentinel-1A Ascending and Descending Orbit Data spanning from October 2017 to September 2023, annual average deformation velocities for three orbits were computed, revealing distinctive patterns illustrated in Figure 7a,b,d. Negative values denote deformation moving away from the satellite, while positive values signify deformation towards the satellite. The deformation velocity for orbit A99 is predominantly negative, with deformation mainly concentrated in the middle part of the landslide, reaching a maximum deformation of −126 mm/year. In contrast, the results for orbit D33 show predominantly positive deformation in the middle and lower parts of the landslide, with a maximum deformation of 62 mm/year, while the upper part exhibits negative deformation, reaching a maximum of −53 mm/year. For orbit D106, except for the toe of the landslide where the deformation is positive with a maximum of 26 mm/year, the rest of the areas show negative values, with a maximum deformation of −86 mm/year. The differing distribution of positive and negative deformation rates between the two descending orbits can primarily be attributed to variations in their incident angles. Upon analysis of the three velocity maps, it is evident that the magnitude of deformation rates in the ascending orbit significantly surpasses those in the descending orbits. The variation in deformation rates between the two descending orbit datasets is influenced mainly by the disparity in their incident angles. The discrepancy in the allocation of positive and negative values in the descending orbit data, as depicted in Figure 5, indicates a discrepancy between the deformation direction of the landslide and the slope's direction.

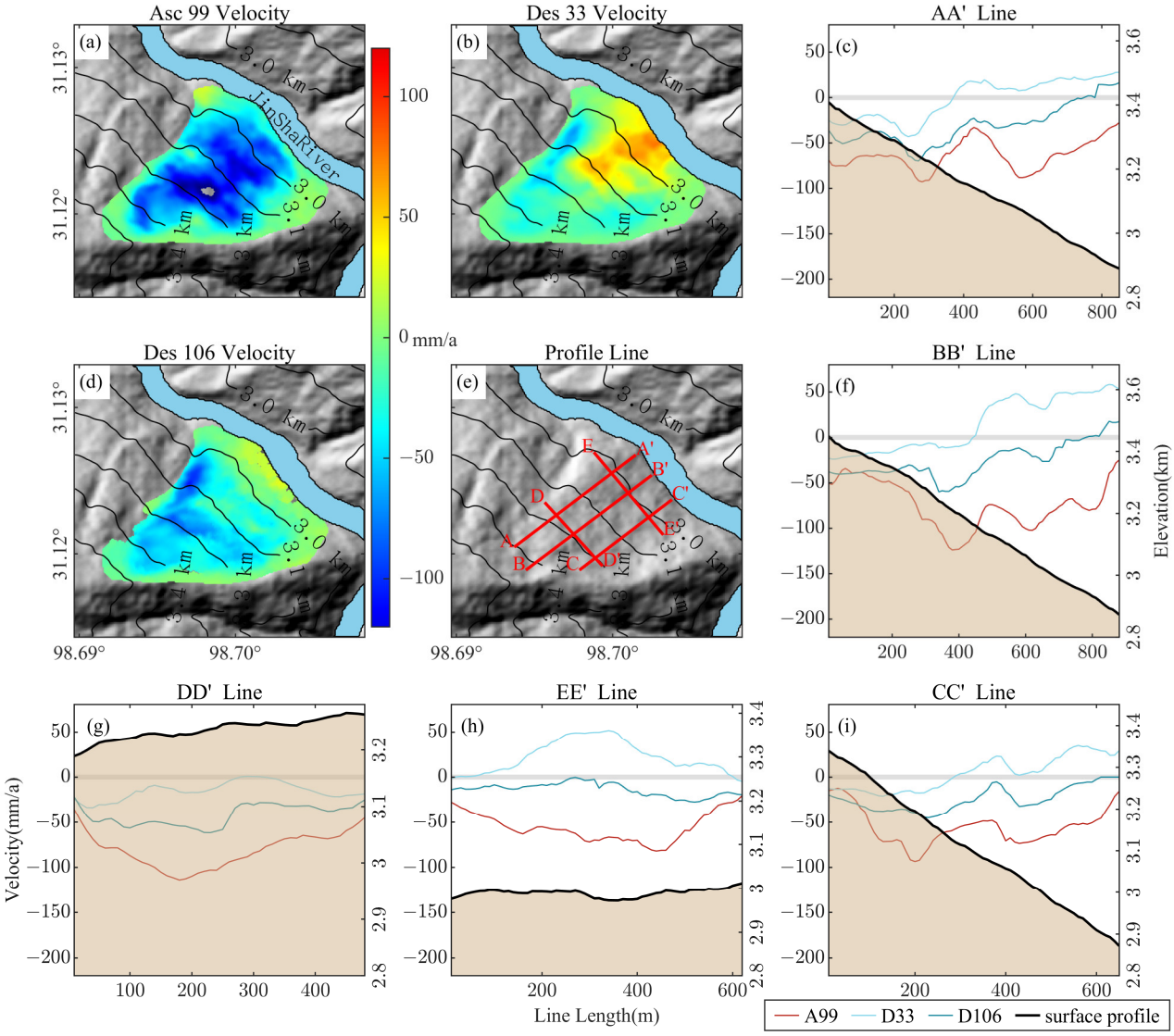

Figure 7. LOS Annual Average Displacement Velocity and Velocity Profile Maps. (**a**,**b**,**d**) Depict the velocity maps for ascending path 99, descending path 33, and descending path 106, respectively. In (**e**), AA′, BB′, and CC′ represent three profiles along the downslope direction, while DD′ and EE′ denote two cross profiles. (**c**,**f**–**i**) Correspond to the velocity distribution maps of the three orbits for profiles AA′, BB′, CC′, DD′, and EE′, respectively.

To further analyze the discrepancies, five cross-sectional profiles were set within the landslide area: three profiles along the downslope direction, AA′, BB′, and CC′, and two transverse profiles, DD′ and EE′. From Figure 7g,h, it can be observed that along the central profile line DD′, the projection of the true motion velocity of the landslide body on the D33 orbit is minimal, followed by D106, with all three orbit results being negative. These results indicate that at DD′, the predominant true deformation of the landslide occurs vertically and is approximately perpendicular to the LOS direction of the D33 orbit. However, in the middle-lower part of the landslide along profile line EE′, the direction of true deformation is approximately perpendicular to the LOS direction of the D106 orbit, with positive values observed on the D33 orbit and negative values projected on the D106 orbit. At EE′, the horizontal deformation of the landslide predominates over the vertical deformation. These conditions arise because the local incidence angle of the D33 orbit is greater than that of D106, resulting in differences in the measured true deformation between the two orbits. Moreover, the distribution of positive and negative projection coefficients in the D106 orbit

in Figure 5 does not match the distribution of positive and negative deformation velocities corresponding to this orbit in Figure 7d. These discrepancies further illustrate that the direction of true displacement does not align with the slope direction, indicating that the surface parallel flow model cannot accurately reproduce the true deformation results of the Xiaomojiu landslide.

In the existing drilling data for the Xiaomojiu landslide [42], the maximum depth of the three boreholes is 60 m, none of which reached the bedrock. Based on the drilling results and other geological and topographical data, the landslide mass is a typical high-steep valley-shaped fragmented and loose structure. From the profiles along the steepest downhill direction shown in Figure 7c,f,i, it can be observed that the landslide deformation exhibits distinct segments. Two main deformation zones within the landslide are located in the upper-middle and lower-middle parts of the slope.

4.2. Temporal Deformation of the Xiaomojiu Landslide

In the simulation study of the Xiaomojiu landslide [42], it was suggested that the Xiaomojiu landslide might block the river and create the risk of forming a barrier lake after its collapse. To further analyze the development characteristics of the landslide, we selected the time-series deformation results of four points at different heights in the center of the landslide for temporal analysis.

From Figure 8a,c,e, it can be observed that before the occurrence of the Baige landslide damming event, the overall deformation of the landslide was relatively small. However, after the disaster, the Xiaomojiu landslide began to accelerate. Notably, the maximum temporal deformation was observed at point P2 in the upper-middle part of the landslide. Specifically, for point P2, the cumulative deformation from October 2017 to July 2023 was −56 cm for the A99 orbit, −10 cm for the D33 orbit, and −33 cm for the D106 orbit. The differences in deformation magnitudes reflect variations in the projection coefficients of true deformation in different observation directions. Analysis of the cumulative deformation results for the four points indicates that the D33 orbit is less sensitive to deformations in the middle part of the landslide.

In contrast, the D106 orbit is less sensitive to deformations in the lower part. As depicted in Figure 8b, after the Baige landslide damming event, the deformation at points P4 and P3 in the lower-middle part of the landslide initially increased before decreasing. This phenomenon may be attributed to the immersion of the landslide toe in the dammed lake water, resulting in initial deformation at the toe followed by displacement in the middle and lower parts. The transfer of displacement from lower to higher areas exhibits significant lag.

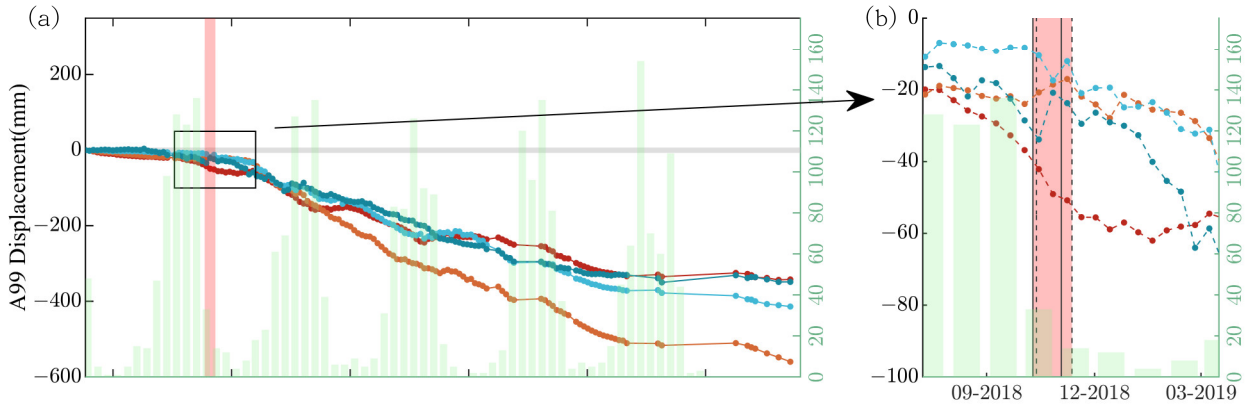

Figure 8. *Cont.*

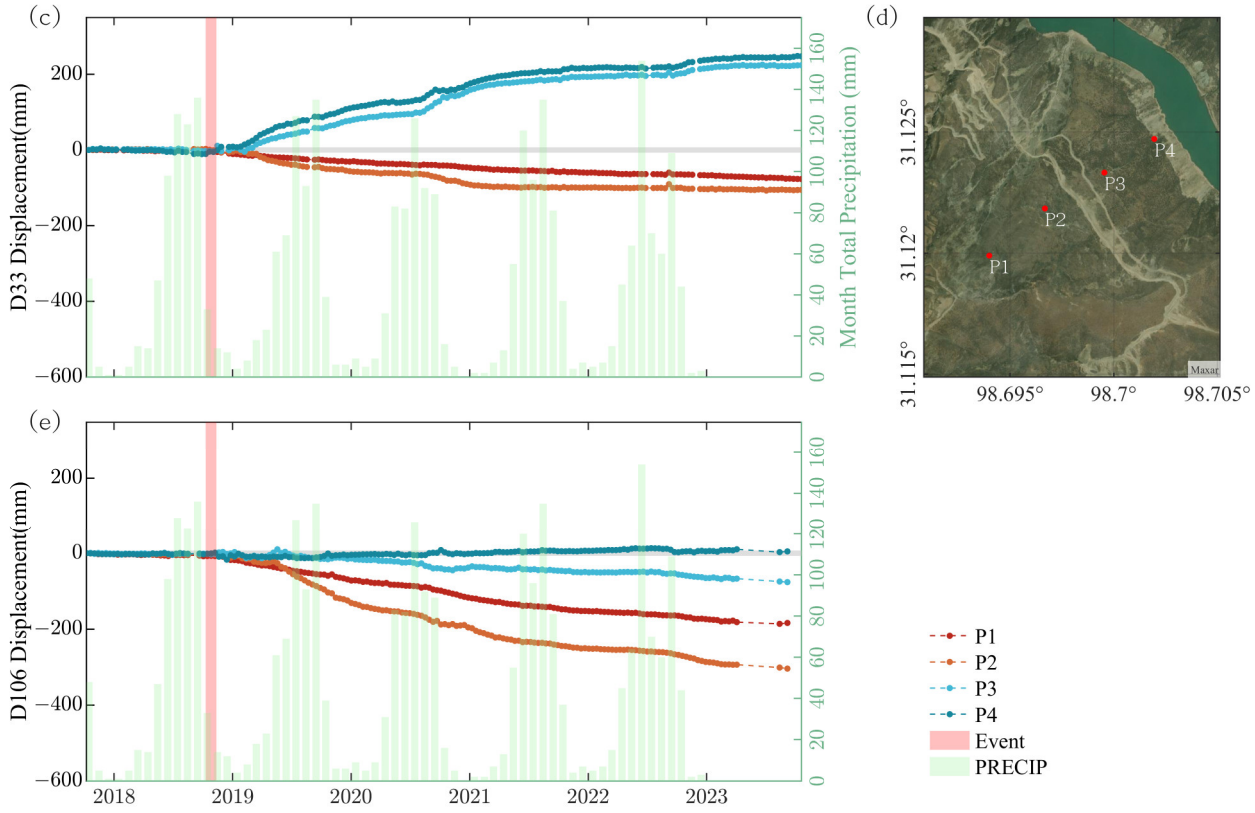

Figure 8. (**a**) P1 to P4 cumulative ascending orbit path 99 temporal cumulative strain map, (**c**) P1 to P4 cumulative descending orbit path 33 temporal cumulative deformation map, (**d**) distribution map of four points P1 to P4, (**e**) P1 to P4 cumulative ascending orbit path 106 temporal cumulative strain map. (**b**) This sub-figure is a magnified view of (**a**), where solid black lines represent the dates of the two failures of the Baige landslide, and black dashed lines represent the dates of the debris flow events from the barrier lake outburst. In all sub-figures, the light red EVENT represents the barrier lake events formed by the two failures of the Baige landslide. PRECIP represents the monthly total precipitation in the region from 2017 to 2022 [49].

5. Analysis and Discussion

5.1. The 3D Deformation Characteristics of the Xiaomojiu Landslide

The actual spatial deformation characteristics of the Xiaomojiu landslide were computed using the methods mentioned in this paper. Considering the relatively long data gap in the ascending orbit data after May 2021, cumulative deformations were calculated from October 2018 to May 2021 using data from three orbits. These results were then compared with those obtained from other methods, such as the SPFM [32], SPFM coupled with the least-squares method (SPF-LSM) [60], and the APFM [62]. The Adjacent Orientation Consistency Model (AOCM) mentioned in this paper does not utilize slope and aspect as the displacement direction for surface deformation. Instead, it solves for the unknown true deformation direction and decomposes the true deformation into the NEU directions, as illustrated in Figure 9.

From the results in Figure 9, it can be observed that the east-west and vertical deformations obtained by various methods exhibit relatively consistent spatial distributions, but there are differences in numerical values. The north-south deformation obtained using AOCM differs significantly from the results obtained by the previous three methods, indicating the presence of some degree of lateral horizontal movement in the middle part of the landslide. These results suggest a disparity between the movement direction of landslide sub-blocks on the landslide body and the overall steepest movement direction. Overall, there is a significant spatial distribution difference in the vertical deformation of

the landslide body, with eastward movement predominating horizontally. In conclusion, optimizing the true deformation displacement using multi-track LOS data can provide more accurate vertical deformation of the landslide body, thereby offering more precise data support for analyzing the profile characteristics of the landslide. To further analyze the landslide structure, we extracted the actual deformation results corresponding to the BB′ profile, including the actual deformation values on the BB′ profile calculated by AOCM and the corresponding angles with the horizontal plane (Figure 10).

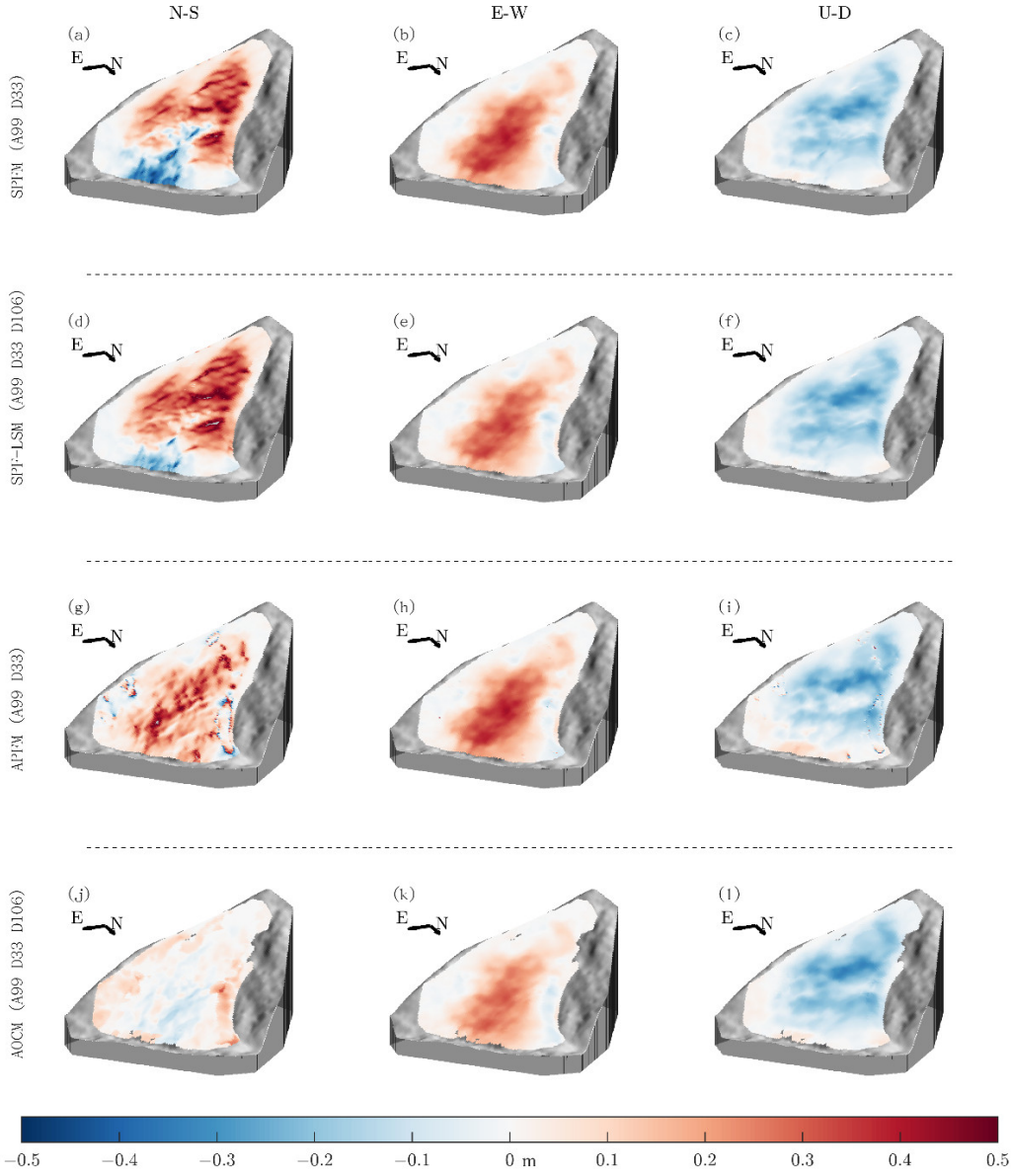

Figure 9. Different methods yield 3D deformation maps of the Xiaomojiu landslide. The first row displays the NEU direction deformation maps computed using the SPFM method: (**a**–**c**). The second row showcases the NEU direction deformation maps computed using the SPF-LSM method: (**d**–**f**). The third row exhibits the NEU direction deformation maps obtained from the APFM method: (**g**–**i**). Finally, the fourth row presents the NEU direction deformation maps calculated using the AOCM method: (**j**–**l**).

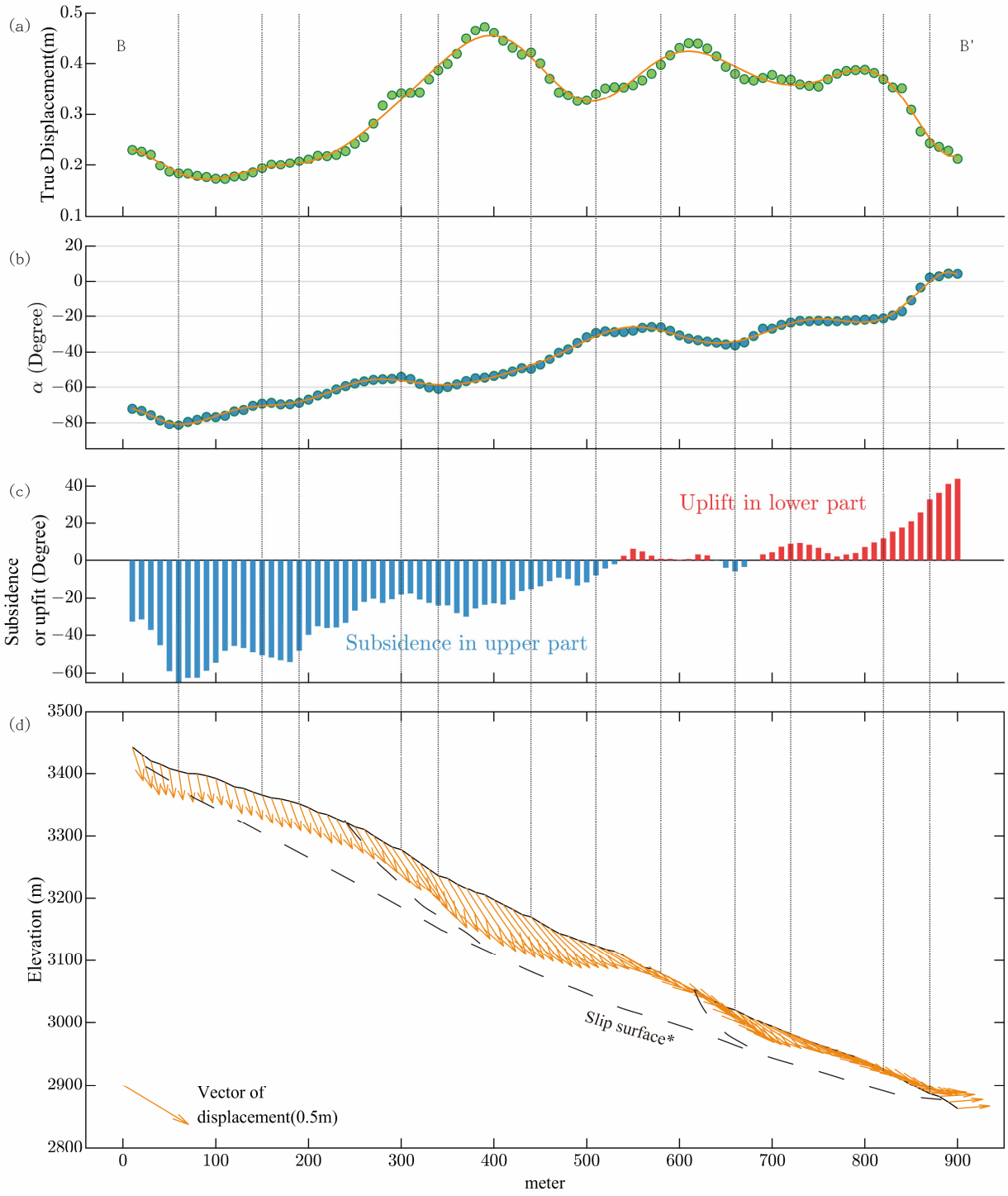

Figure 10. (**a**) Accumulated true deformation along profile BB′ (from October 2018 to May 2021), (**b**) angle between the true deformation direction along profile BB′ and the horizontal plane, (**c**) deviation between the corresponding inclination angle along profile BB′ and the negative slope angle, (**d**) the distribution of displacement vectors along profile BB′ is illustrated, with vertical dashed lines employed to delineate variations in angles. The dashed line (slip surface*) indicates the inferred sliding surface derived from prior research and computational outcomes.

The displacement on the landslide profile reflects the main movement characteristics of the landslide body. Figure 10a shows that the landslide body exhibits three deformation peaks concentrated in the middle-lower part of the landslide. The maximum deformation peak is located in the middle part of the landslide, with a cumulative deformation of 0.47 m. In contrast, the upper part primarily experiences vertical movement, with a cumulative deformation of approximately 0.2 m. Figure 10b indicates that the middle-lower part is subjected to compression from the upper part, resulting in the most significant degree of deformation. Figure 10b,c depict changes in the direction of surface movement of the landslide body. The average angle α of the upper part is approximately 70°, with deformation primarily manifested as subsidence, resulting in compression in the middle part. The angle α gradually approaches horizontal from the middle to the toe, while deformation gradually decreases, indicating a change in stress state and increased frictional resistance. These angular changes suggest the presence of an arc-shaped sliding zone within the landslide body. Additionally, at least two main landslide sub-blocks correspond to two arc-shaped sliding surfaces in the middle-lower part of the landslide, resulting in the superposition of landslide subzones and a pronounced toe extrusion phenomenon.

For further analysis of the landslide area, the real deformation direction, magnitude, and spatial information of each point obtained using the methods mentioned in this study were utilized as features. The K-means method [64] was employed for cluster analysis, and based on the elbow method, the landslide was divided into 12 sub-blocks, as shown in Figure 11b. For the five landslide sub-block regions located along the central axis (C12, C9, C8, C5, C2), each region's pixel points correspond to two angles, alpha and beta, representing the actual deformation directions. The magnitudes of these angles exhibit a relatively concentrated distribution. This result indicates that within each sub-block region, the actual displacement directions of each pixel are closely aligned (Figure 12a,b). When the deformation within the sub-block was relatively small, such as in the case of the C11 and C3 sub-blocks, the estimated real displacement direction within the sub-block was more dispersed, and the standard deviation of the actual deformation obtained was also more prominent.

Additionally, the overall direction of the slope in the C4 area was close to the north direction, consistent with the actual terrain distribution. The horizontal directions in the remaining areas were relatively similar except for the C3, C4, and C11. From the results of the average temporal cumulative deformation, it can be observed that among the C2, C5, and C8 sub-blocks arranged from low to high elevation, after the occurrence of the damming event, the bottom C2 sub-block began accelerating movement first, followed by a certain lag in the C5 sub-block at a higher elevation, with the C8 sub-block showing even longer lag time. This distribution indicates that the damming event progressively influenced the landslide activation from low to high elevations in a chain reaction along the altitude.

Considering the calculated 3D features of the landslide sub-blocks, it can be observed that the lower-middle parts of the landslide, represented by sub-blocks C8 and C5, exhibit characteristics of rotational sliding surfaces, consistent with the two rotational sliding sub-zones mentioned earlier. This phenomenon corresponds to the thick accumulation layers within the landslide body. In addition to the overall movement of the Xiaomojiu landslide, the presence of these two sliding sub-zones adds complexity to the landslide morphology and diversifies the sliding patterns. Consequently, during the subsequent continuous deformation of the landslide, the instability of the landslide body is increased.

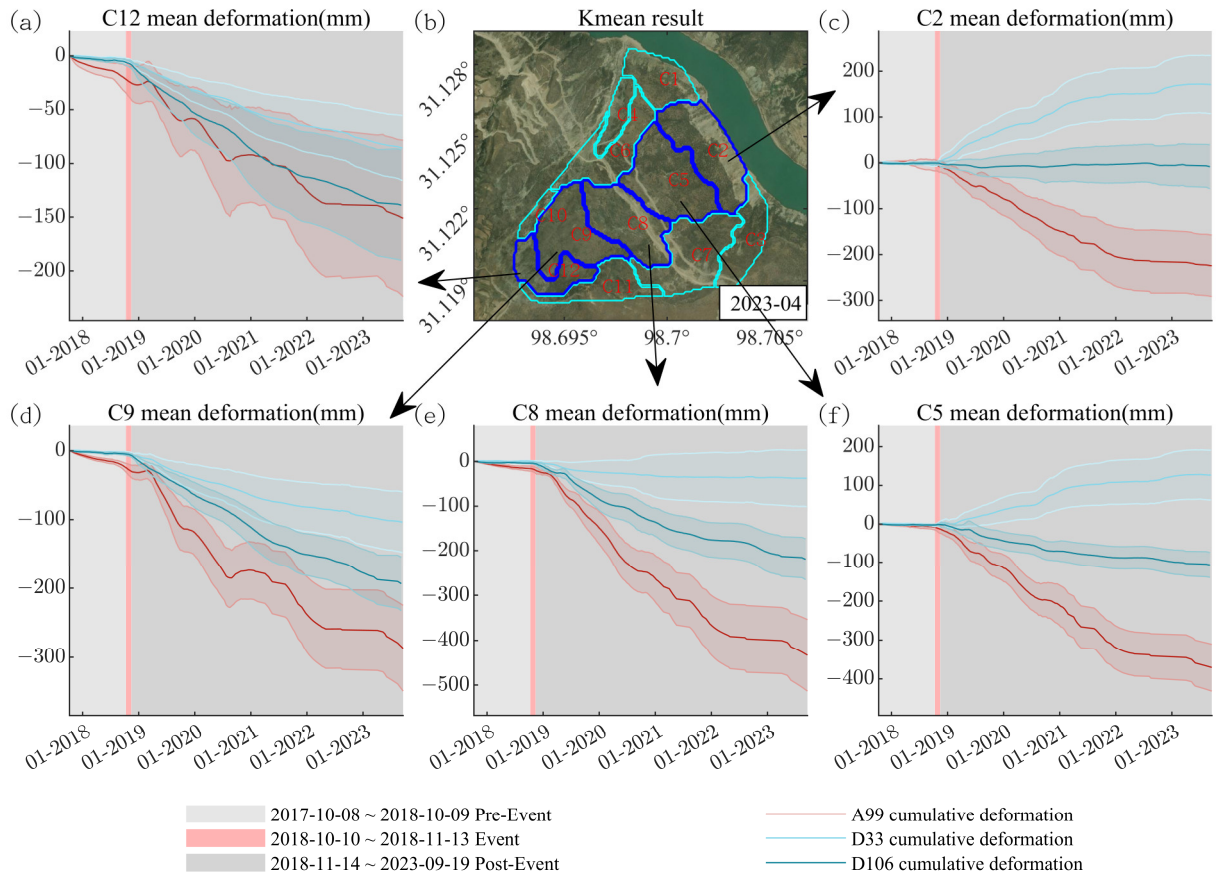

Figure 11. K-means clustering results of landslide blocks and typical multi-track average temporal results; trends of average cumulative deformation for landslide blocks across three orbits, (**a**) Block C12, (**c**) Block C2, (**d**) Block C9, (**e**) Block C8, (**f**) Block C5. The temporal data's light-colored upper and lower bounds represent the standard deviation range. (**b**) Spatial distribution map of clustering results.

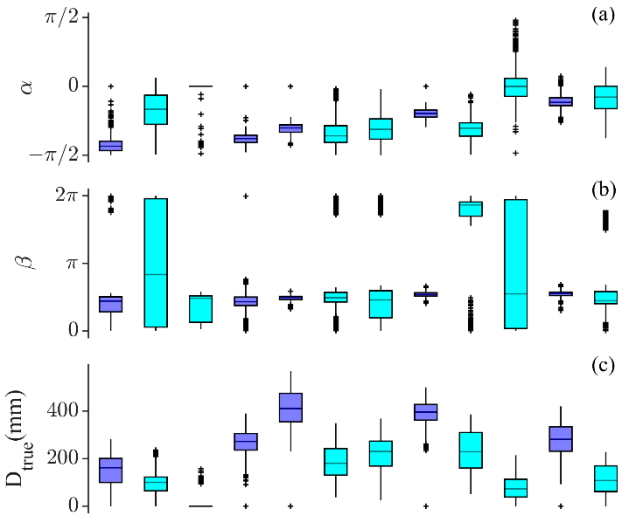

Figure 12. *Cont.*

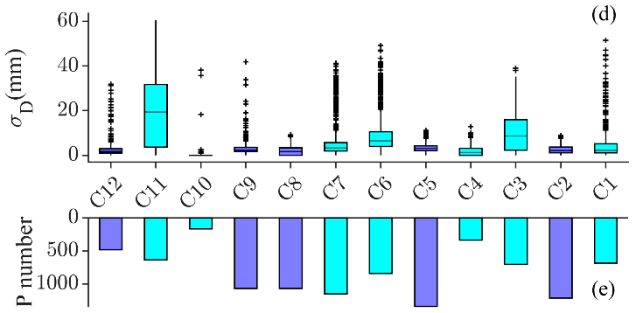

Figure 12. Box plots of the actual deformation characteristics within sub-blocks obtained from K-means clustering, (**a**) comparative distribution of angle α in different sub-block regions, (**b**) comparative distribution of angle β in different sub-block regions, (**c**) comparative distribution of angle D_{true} in different sub-block regions, (**d**) comparative distribution of standard deviation D_{true} in different sub-block regions, (**e**) comparative distribution of the number of ground points in different sub-block regions.

5.2. The Driving Factors of the Xiaomijiu Landslide Movement

To analyze the impact of changes in river water level caused by the damming lake event on the landslide movement process, intensity images of D33 descending orbit VH and VV polarization were used as the data source. The Block Matching 3D algorithm (BM3D) filtering method [65] was employed to filter the selected intensity image data, removing speckle noise. Time-series charts of water area extraction from the beginning of the Xiaomojiu landslide to the upstream river were generated to indirectly represent changes in river water level. Considering the significant surface undulations in the area and the presence of many shadow regions in the intensity images, masking was applied to avoid the influence of shadow areas on the delineation of water bodies. Additionally, river buffer zones were delineated based on elevation information, and the threshold segmentation method [66] was utilized to delineate water bodies within the buffer zones. Comparing Figure 13b,c, it is evident that the water area increased after the damming lake event. As shown in Figure 13c, the acquisition time of the D33 orbit data was UTC 23:21 on 10 October 2018, approximately 9 h after the Baige landslide had dammed the lake, resulting in a significant rise in water level.

The temporal results of the water body area (Figure 13e) reflect the following points. Firstly, following the formation of the landslide dam, the water area upstream of the Baige landslide rapidly increased, indicating a swift rise in the upstream water level due to the damming event. During the landslide dam occurrence, the water area underwent two cycles of increase followed by a decrease, corresponding to the two damming events and consistent with the cumulative deformation results in Figure 8b. Secondly, in the aftermath of the damming events, the water area upstream did not return to its pre-event level, indicating that the remaining debris from the landslide blocked the river channel, causing a certain degree of elevation in the water level upstream. Additionally, erosion and immersion of the upstream river channel might have occurred during the damming events, leading to the widening of the river channel. Thirdly, after the release of the landslide dam, the elevated water level in the upstream river channel was in an overall slow declining state. Therefore, the overall movement characteristics of the Xiaomojiu landslide are closely related to changes in the water level of the Jinsha River after being activated.

Furthermore, upon further comparison with optical data in Figure 14, it can be observed that due to immersion from the damming lake and erosion by the river water, the exposed area of the Xiaomojiu landslide toe gradually increased. Figure 14a,c,h demonstrate the comparison of river channels during the same season. After the Baige landslide event, the width of the river channel noticeably increased, consistent with the temporal results representing the pixel count of the river channel in Figure 13e.

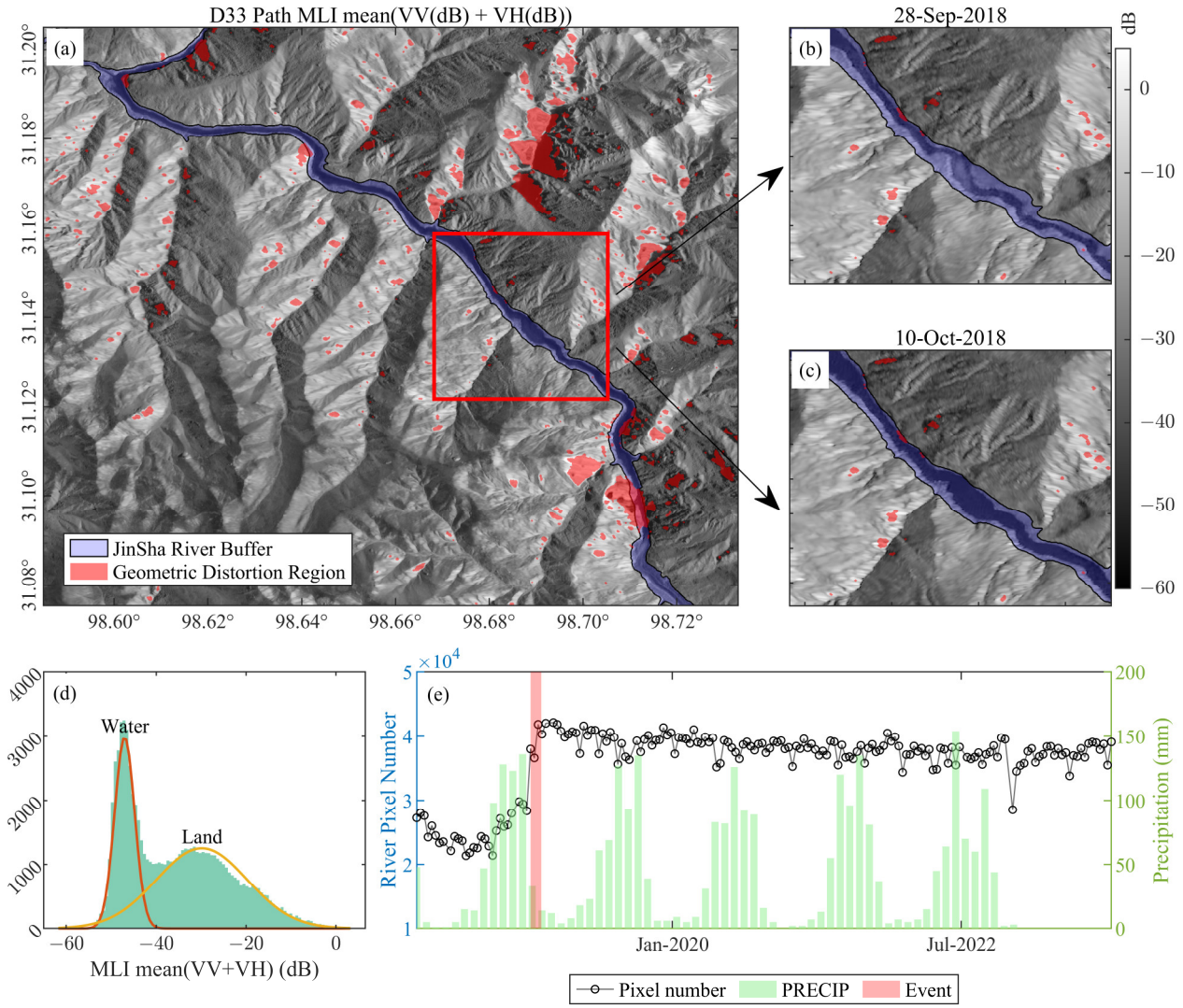

Figure 13. (**a**) Overlay image of D33 orbit VV and VH backscatter images (in dB), with the light purple area representing the river buffer zone generated based on elevation. (**b**) Partial VV+VH image before the first occurrence of the Baige landslide damming lake on 28 September 2018. (**c**) Partial VV+VH image two hours after the first occurrence of the Baige landslide damming lake on 10 October 2018. (**d**) Distribution map of pixel values within the river buffer zone, where the first peak represents water bodies, and the second peak represents land. (**e**) The time series plot of the total pixel count within the river buffer zone was calculated using the threshold segmentation method.

According to the time-series results of the water area shown in Figure 13e, the following conclusions can be drawn: Firstly, after the barrier lake event, the water area in the upstream region of the Baige landslide expanded rapidly, indicating a swift rise in water level upstream due to the impact of the barrier lake. During the barrier lake event, the quantity of water area experienced two increases followed by decreases, corresponding to the two occurrences of the barrier lake. The changes in water level are consistent with the cumulative deformation results shown in Figure 8b. Secondly, following the damming lake event, the water area in the upstream area did not return to the pre-event level, indicating that the remaining debris from the Baige landslide blocked the river channel to some extent, raising the water level in the upstream area. Additionally, channel widening may have been due to erosion and immersion during the damming lake event. Thirdly, after the damming lake was discharged, the elevated water level in the upstream channel of the Baige landslide gradually decreased overall. Therefore, after being activated, the overall

movement characteristics of the Xiaomojiu landslide are closely related to the changes in the Jinsha River water level.

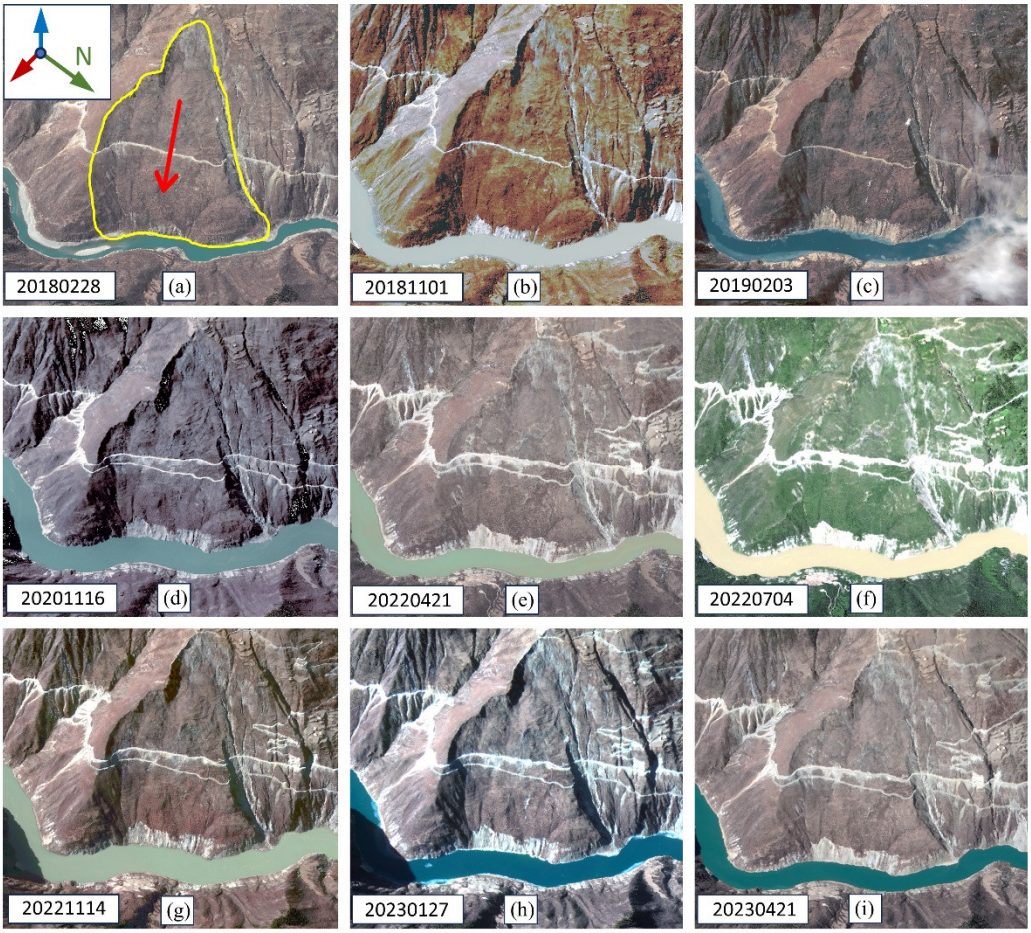

Figure 14. Shows optical remote sensing images from the GF-2 satellite on 28 February 2018 (**a**), 1 February 2019 (**c**), 16 November 2020 (**d**), 21 April 2022 (**e**), 4 July 2022 (**f**), 14 November 2022 (**g**), 27 January 2023 (**h**), and 21 April 2023 (**i**). Another optical remote sensing image was taken from a GF-7 satellite on 1 November 2018 (**b**).

Due to the influence of the residual accumulation of the Baige landslide on the water level in the upstream channel, the moisture content within the landslide has changed. Prolonged higher water levels can cause a redistribution of water within the landslide, increasing the soil moisture content and reducing its shear strength, thereby accelerating the deformation process of the landslide. Results obtained through InSAR technology reveal that the upper part of the Xiaomojiu landslide is undergoing subsidence, while the bottom part is experiencing extrusion and uplift. This deformation pattern indicates a redistribution of internal stresses within the landslide when subjected to external forces. Furthermore, the presence of two sub-blocks in the lower part of the landslide exhibiting characteristics similar to soil-rotational landslides further complicates the movement characteristics of the landslide mass. These sub-blocks may play a critical role in the overall stability of the landslide during its movement process, influencing its overall stability. In conclusion, the Xiaomojiu landslide is a deep-seated accumulation creep-type landslide formed under complex geological conditions and external influences. Reactivated and continuously deforming due to the rise in river water levels, the landslide remains in a phase of sustained deformation.

6. Conclusions

In this study, we propose a method based on the consistency constraint of neighboring directions to invert the true deformation displacement. Utilizing three-track cumulative deformation data calculated by SBAS-InSAR, we invert the true deformation of the landslide body. Compared to methods that pre-determine the direction of landslide movement, the proposed method in this study more accurately reflects the true movement characteristics of the landslide body. Based on this, we draw the following conclusions when analyzing the Xiaomojiu landslide movement.

(1) This study presents the results of SBAS-InSAR technology to obtain multi-track LOS velocity data of the Xiaomojiu landslide. From 2017 to 2023, the maximum LOS displacement rate of the Xiaomojiu landslide was found to be −126 mm/yr. Variations in the C-index values and the distribution of LOS velocity signs differ among the orbits, suggesting that the motion pattern of the Xiaomojiu landslide does not fit the translation-type landslide model. This difference indicates a significant discrepancy between the true displacement direction of the Xiaomojiu landslide body's surface and the deformation direction calculated based on the surface slope. The vertical deformation is further constrained by utilizing the LOS observations from three orbits. The proposed method in this study provides a more accurate real displacement vector of the landslide motion compared to several surface parallel flow methods.

(2) Large landslides typically exhibit complex movement characteristics. By analyzing the angle distribution along the profile line, it is evident that the upper part of the Xiaomojiu landslide is mainly dominated by downward movement. The sinking in the upper part compresses the middle part of the landslide, resulting in the most significant deformation in the middle, while the bottom part shows extrusion phenomena. Additionally, two rotational sliding zones are present in the lower part of the landslide. The landslide area is partitioned using the K-means classification method based on the 3D deformation features. The two rotational sliding zones correspond to the C8 and C5 blocks obtained from the classification, indicating the complexity of the Xiaomojiu landslide structure.

(3) In analyzing driving factors for the movement of the Xiaomojiu landslide, we extracted the water area of certain rivers in the study area using Sentinel-1 intensity information. Changes in water areas can reflect changes in water levels to some extent. The activation of the landslide body due to the debris dam event occurs gradually from low to high elevations, with a phenomenon of deformation lag. Following the event, the upstream water level remains consistently high for an extended period, gradually decreasing. This state has profound implications for the landslide body, maintaining it in continuous deformation.

In this study, the proposed method is a practical approach for accurately measuring surface deformation in landslides characterized by intricate sliding surfaces without assuming the direction of movement. However, a fundamental limitation of this method is its reliance on a minimum of three observation tracks, which constrains its applicability. Moreover, the method's utility is further compromised by the inherent constraints of InSAR technology, particularly in managing substantial displacement and rapid accelerations during landslide events. By integrating the Xiaomojiu calculation outcomes with the specific topographic and geological features of the landslide area, it is deduced that the Xiaomojiu landslide exhibits characteristics of a deep-seated accumulation-type creep landslide with a complex movement pattern. The continuous water-driven influence poses a considerable destabilization risk to the landslide area, underscoring the critical necessity for intensified deformation monitoring and comprehensive ground surveys.

Author Contributions: Conceptualization, X.M. and J.P.; methodology, X.M.; validation, X.M., Y.S. and M.S.; investigation, X.M., Y.Z. and X.L.; data curation, X.M. and X.J.; writing—original draft preparation, X.M.; writing—review and editing, X.M., M.S. and Y.S.; visualization, X.M.; supervision, J.P., Y.S. and M.S.; funding acquisition, J.P. All authors have read and agreed to the published version of the manuscript.

Funding: This research was funded by the National Natural Science Foundation of China under Grant 42074004 and in part by Shanxi Transportation Holdings Group, Company, Ltd., under Grant 19-JKKJ-3.

Data Availability Statement: The Sentinel-1 data have been made freely available by the European Space Agency and distributed and archived by the Alaska Satellite Facility, https://www.asf.alaska.edu/sentinel/, (accessed on 4 November 2023); Precise Orbit Ephemerides (POD) used in this study were provided by the ESA, https://scihub.copernicus.eu/gnss/#/home (accessed on 4 November 2023); and the AW3D DEM was freely downloaded from the website https://opentopography.org/ (accessed on 4 November 2023). Meteorological observation data are provided by National Tibetan Plateau Data Center http://data.tpdc.ac.cn, (accessed on 4 November 2023).

Acknowledgments: The authors thank the European Space Agency (ESA) for providing Sentinel-1 SAR data. The optical image data were kindly provided by AGRS.

Conflicts of Interest: The authors declare no conflicts of interest.

References

1. Wang, J.B.; Lei, T.J.; Liu, W.K.; Chen, Y.J.; Yue, J.W.; Liu, B.Y. Prediction analysis of landslide displacement trajectory based on the gradient descent method with multisource remote sensing observations. *Geomat. Nat. Hazards Risk* **2023**, *14*, 143–175. [CrossRef]
2. Xiong, Z.Q.; Zhang, M.Z.; Ma, J.; Xing, G.L.; Feng, G.C.; An, Q. InSAR-based landslide detection method with the assistance of C-index. *Landslides* **2023**, *20*, 2709–2723. [CrossRef]
3. Haque, U.; da Silva, P.F.; Devoli, G.; Pilz, J.; Zhao, B.X.; Khaloua, A.; Wilopo, W.; Andersen, P.; Lu, P.; Lee, J.; et al. The human cost of global warming: Deadly landslides and their triggers (1995–2014). *Sci. Total Environ.* **2019**, *682*, 673–684. [CrossRef] [PubMed]
4. Du, J.; Glade, T.; Woldai, T.; Chai, B.; Zeng, B. Landslide susceptibility assessment based on an incomplete landslide inventory in the Jilong Valley, Tibet, Chinese Himalayas. *Eng. Geol.* **2020**, *270*, 105572. [CrossRef]
5. Fan, X.M.; Xu, Q.; Alonso-Rodriguez, A.; Subramanian, S.S.; Li, W.L.; Zheng, G.; Dong, X.J.; Huang, R.Q. Successive landsliding and damming of the Jinsha River in eastern Tibet, China: Prime investigation, early warning, and emergency response. *Landslides* **2019**, *16*, 1003–1020. [CrossRef]
6. Liu, X.J.; Zhao, C.Y.; Zhang, Q.; Lu, Z.; Li, Z.H.; Yang, C.S.; Zhu, W.; Liu-Zeng, J.; Chen, L.Q.; Liu, C.J. Integration of Sentinel-1 and ALOS/PALSAR-2 SAR datasets for mapping active landslides along the Jinsha River corridor, China. *Eng. Geol.* **2021**, *284*, 106033. [CrossRef]
7. Yang, Z.W.; Liu, W.M.; Garcia-Castellanos, D.; Ruan, H.C.; Luo, J.P.; Zhou, Y.L.; Sang, Y.Y. Geomorphic response of outburst floods: Insight from numerical simulations and observations-The 2018 Baige outburst flood in the upper Yangtze River. *Sci. Total Environ.* **2022**, *851*, 158378. [CrossRef] [PubMed]
8. Ouyang, C.J.; An, H.C.; Zhou, S.; Wang, Z.W.; Su, P.C.; Wang, D.P.; Cheng, D.X.; She, J.X. Insights from the failure and dynamic characteristics of two sequential landslides at Baige village along the Jinsha River, China. *Landslides* **2019**, *16*, 1397–1414. [CrossRef]
9. Zhang, Z.; He, S.M.; Liu, W.; Liang, H.; Yan, S.X.; Deng, Y.; Bai, X.Q.; Chen, Z. Source characteristics and dynamics of the October 2018 Baige landslide revealed by broadband seismograms. *Landslides* **2019**, *16*, 777–785. [CrossRef]
10. FENG, W.; ZHANG, G.; BAI, H.; ZHOU, Y.; XU, Q.; ZHENG, G. A preliminary analysis of the formation mechanism and development tendency of the huge Baige landslide in Jinsha River on October 11, 2018. *J. Eng. Geol.* **2019**, *27*, 415–425. [CrossRef]
11. Gao, Y.J.; Zhao, S.Y.; Deng, J.H.; Yu, Z.Q.; Rahman, M. Flood assessment and early warning of the reoccurrence of river blockage at the Baige landslide. *J. Geogr. Sci.* **2021**, *31*, 1694–1712. [CrossRef]
12. Tian, S.F.; Chen, N.S.; Wu, H.; Yang, C.Y.; Zhong, Z.; Rahman, M. New insights into the occurrence of the Baige landslide along the Jinsha River in Tibet. *Landslides* **2020**, *17*, 1207–1216. [CrossRef]
13. Casagli, N.; Intrieri, E.; Tofani, V.; Gigli, G.; Raspini, F. Landslide detection, monitoring and prediction with remote-sensing techniques. *Nat. Rev. Earth Environ.* **2023**, *4*, 51–64. [CrossRef]
14. Torres, R.; Snoeij, P.; Geudtner, D.; Bibby, D.; Davidson, M.; Attema, E.; Potin, P.; Rommen, B.; Floury, N.; Brown, M.; et al. GMES Sentinel-1 mission. *Remote Sens. Environ.* **2012**, *120*, 9–24. [CrossRef]
15. Su, Y.; Peng, J.; Shi, M.; Guo, C.; Ma, X.; Li, X.; Wang, J.; Wang, W. An M-Estimation Method for InSAR Nonlinear Deformation Modeling and Inversion. *IEEE Trans. Geosci. Remote Sens.* **2024**, *62*, 1–12. [CrossRef]
16. Zhao, C.; Lu, Z. Remote Sensing of Landslides—A Review. *Remote Sens.* **2018**, *10*, 279. [CrossRef]
17. Miano, A.; Mele, A.; Calcaterra, D.; Martire, D.D.; Infante, D.; Prota, A.; Ramondini, M. The use of satellite data to support the structural health monitoring in areas affected by slow-moving landslides: A potential application to reinforced concrete buildings. *Struct. Health Monit.* **2021**, *20*, 3265–3287. [CrossRef]
18. Solari, L.; Del Soldato, M.; Raspini, F.; Barra, A.; Bianchini, S.; Confuorto, P.; Casagli, N.; Crosetto, M. Review of Satellite Interferometry for Landslide Detection in Italy. *Remote Sens.* **2020**, *12*, 1351. [CrossRef]
19. Xiong, Z.Q.; Feng, G.C.; Feng, Z.X.; Miao, L.; Wang, Y.D.; Yang, D.J.; Luo, S.R. Pre- and post-failure spatial-temporal deformation pattern of the Baige landslide retrieved from multiple radar and optical satellite images. *Eng. Geol.* **2020**, *279*, 105880. [CrossRef]
20. Intrieri, E.; Frodella, W.; Raspini, F.; Bardi, F.; Tofani, V. Using Satellite Interferometry to Infer Landslide Sliding Surface Depth and Geometry. *Remote Sens.* **2020**, *12*, 1462. [CrossRef]

21. Liu, X.J.; Zhao, C.Y.; Zhang, Q.; Yin, Y.P.; Lu, Z.; Samsonov, S.; Yang, C.S.; Wang, M.; Tomás, R. Three-dimensional and long-term landslide displacement estimation by fusing C- and L-band SAR observations: A case study in Gongjue County, Tibet, China. *Remote Sens. Environ.* **2021**, *267*, 112745. [CrossRef]
22. Eriksen, H.O.; Lauknes, T.R.; Larsen, Y.; Corner, G.D.; Bergh, S.G.; Dehls, J.; Kierulf, H.P. Visualizing and interpreting surface displacement patterns on unstable slopes using multi-geometry satellite SAR interferometry (2D InSAR). *Remote Sens. Environ.* **2017**, *191*, 297–312. [CrossRef]
23. Hu, J.; Li, Z.W.; Ding, X.L.; Zhu, J.J.; Zhang, L.; Sun, Q. Resolving three-dimensional surface displacements from InSAR measurements: A review. *Earth-Sci. Rev.* **2014**, *133*, 1–17. [CrossRef]
24. Zhang, C.L.; Li, Z.H.; Yu, C.; Chen, B.; Ding, M.T.; Zhu, W.; Yang, J.; Liu, Z.J.; Peng, J.B. An integrated framework for wide-area active landslide detection with InSAR observations and SAR pixel offsets. *Landslides* **2022**, *19*, 2905–2923. [CrossRef]
25. Bechor, N.B.D.; Zebker, H.A. Measuring two-dimensional movements using a single InSAR pair. *Geophys. Res. Lett.* **2006**, *33*. [CrossRef]
26. Del Soldato, M.; Confuorto, P.; Bianchini, S.; Sbarra, P.; Casagli, N. Review of Works Combining GNSS and InSAR in Europe. *Remote Sens.* **2021**, *13*, 1684. [CrossRef]
27. Meng, Q.; Li, W.; Raspini, F.; Xu, Q.; Peng, Y.; Ju, Y.; Zheng, Y.; Casagli, N. Time-series analysis of the evolution of large-scale loess landslides using InSAR and UAV photogrammetry techniques: A case study in Hongheyan, Gansu Province, Northwest China. *Landslides* **2020**, *18*, 251–265. [CrossRef]
28. Lombardi, L.; Nocentini, M.; Frodella, W.; Nolesini, T.; Bardi, F.; Intrieri, E.; Carlà, T.; Solari, L.; Dotta, G.; Ferrigno, F.; et al. The Calatabiano landslide (southern Italy): Preliminary GB-InSAR monitoring data and remote 3D mapping. *Landslides* **2016**, *14*, 685–696. [CrossRef]
29. Su, Y.; Yang, H.; Peng, J.; Liu, Y.; Zhao, B.; Shi, M. A Novel Near-Real-Time GB-InSAR Slope Deformation Monitoring Method. *Remote Sens.* **2022**, *14*, 5585. [CrossRef]
30. Samsonov, S. Three-dimensional deformation time series of glacier motion from multiple-aperture DInSAR observation. *J. Geod.* **2019**, *93*, 2651–2660. [CrossRef]
31. Baum, R.L.; Messerich, J.; Fleming, R.W. Surface deformation as a guide to kinematics and three-dimensional shape of slow-moving, clay-rich landslides, Honolulu, Hawaii. *Environ. Eng. Geosci.* **1998**, *4*, 283–306. [CrossRef]
32. Ren, K.; Yao, X.; Li, R.; Zhou, Z.; Yao, C.; Jiang, S. 3D displacement and deformation mechanism of deep-seated gravitational slope deformation revealed by InSAR: A case study in Wudongde Reservoir, Jinsha River. *Landslides* **2022**, *19*, 2159–2175. [CrossRef]
33. Samsonov, S.; Dille, A.; Dewitte, O.; Kervyn, F.; d'Oreye, N. Satellite interferometry for mapping surface deformation time series in one, two and three dimensions: A new method illustrated on a slow-moving landslide. *Eng. Geol.* **2020**, *266*, 105471. [CrossRef]
34. He, L.M.; Pei, P.K.; Zhang, X.N.; Qi, J.; Cai, J.Y.; Cao, W.; Ding, R.B.; Mao, Y.C. Sensitivity Evaluation of Time Series InSAR Monitoring Results for Landslide Detection. *Remote Sens.* **2023**, *15*, 3906. [CrossRef]
35. Xia, Z.G.; Motagh, M.; Li, T.; Peng, M.M.; Roessner, S. A methodology to characterize 4D post-failure slope instability dynamics using remote sensing measurements: A case study of the Aniangzhai landslide in Sichuan, Southwest China. *Isprs J. Photogramm. Remote Sens.* **2023**, *196*, 402–414. [CrossRef]
36. Ma, S.Y.; Qiu, H.J.; Zhu, Y.R.; Yang, D.D.; Tang, B.Z.; Wang, D.Z.; Wang, L.Y.; Cao, M.M. Topographic Changes, Surface Deformation and Movement Process before, during and after a Rotational Landslide. *Remote Sens.* **2023**, *15*, 662. [CrossRef]
37. Zhang, S.; Fan, Q.; Niu, Y.; Qiu, S.; Si, J.; Feng, Y.; Zhang, S.; Song, Z.; Li, Z. Two-dimensional deformation monitoring for spatiotemporal evolution and failure mode of Lashagou landslide group, Northwest China. *Landslides* **2022**, *20*, 447–459. [CrossRef]
38. Carter, M.; Bentley, S.P. The Geometry of Slip Surfaces beneath Landslides—Predictions from Surface Measurements. *Can. Geotech. J.* **1985**, *22*, 234–238. [CrossRef]
39. Hungr, O.; Leroueil, S.; Picarelli, L. The Varnes classification of landslide types, an update. *Landslides* **2013**, *11*, 167–194. [CrossRef]
40. Hu, G.S.; Tian, S.F.; Chen, N.S.; Liu, M.; Somos-Valenzuela, M. An effectiveness evaluation method for debris flow control engineering for cascading hydropower stations along the Jinsha River, China. *Eng. Geol.* **2020**, *266*, 105472. [CrossRef]
41. Guo, C.; Yan, Y.; Zhang, Y.; Wu, R.; Yang, Z.; Li, X.; Ren, S.; Zhang, Y.; Wu, Z.; Liu, J. Research progress and prospect of the failure mechanism of large deep-seated creeping landslides in the Tibetan Plateau, China. *Earth Sci.* **2022**, *47*, 3677–3700.
42. Zhang, C.L.; Li, Z.H.; Ding, M.T.; Zhu, W.; Chen, B.; Zhuang, J.Q.; Du, J.T.; Peng, J.B. Dynamic deformation monitoring and scenario simulation of the Xiaomojiu landslide in the Jinsha River Basin, China. *Landslides* **2023**, *20*, 2343–2358. [CrossRef]
43. Cao, W.T.; Yan, D.P.; Qiu, L.; Zhang, Y.X.; Qiu, J.W. Structural style and metamorphic conditions of the Jinshajiang metamorphic belt: Nature of the Paleo-Jinshajiang orogenic belt in the eastern Tibetan Plateau. *J. Asian Earth Sci.* **2015**, *113*, 748–765. [CrossRef]
44. Chen, Z.; Zhou, H.F.; Ye, F.; Liu, B.; Fu, W.X. The characteristics, induced factors, and formation mechanism of the 2018 Baige landslide in Jinsha River, Southwest China. *Catena* **2021**, *203*, 105337. [CrossRef]
45. Liu, X.; Yao, X.; Yao, J. Accelerated Movements of Xiaomojiu Landslide Observed with SBAS-InSAR and Three-Dimensional Measurements, Upper Jinsha River, Eastern Tibet. *Appl. Sci.* **2022**, *12*, 9758. [CrossRef]
46. Liu, D.; Cui, Y.; Wang, H.; Jin, W.; Wu, C.; Bazai, N.A.; Zhang, G.; Carling, P.A.; Chen, H. Assessment of local outburst flood risk from successive landslides: Case study of Baige landslide-dammed lake, upper Jinsha river, eastern Tibet. *J. Hydrol.* **2021**, *599*, 126294. [CrossRef]

47. Zhang, J.; Tang, H.; Li, C.; Gong, W.; Zhou, B.; Zhang, Y. Deformation stage division and early warning of landslides based on the statistical characteristics of landslide kinematic features. *Landslides* **2024**, *21*, 717–735. [CrossRef]
48. Takaku, J.; Tadono, T.; Doutsu, M.; Ohgushi, F.; Kai, H. Updates of 'Aw3d30' Alos Global Digital Surface Model with Other Open Access Datasets. *Int. Arch. Photogramm. Remote Sens. Spat. Inf. Sci.* **2020**, *XLIII-B4-2020*, 183–189. [CrossRef]
49. Shouzhang, P. 1-km monthly precipitation dataset for China (1901–2021). *Earth Syst. Sci. Data* **2020**, *4*, 1931–1946. [CrossRef]
50. Berardino, P.; Fornaro, G.; Lanari, R.; Sansosti, E. A new algorithm for surface deformation monitoring based on small baseline differential SAR interferograms. *Ieee Trans. Geosci. Remote Sens.* **2002**, *40*, 2375–2383. [CrossRef]
51. Pepe, A.; Lanari, R. On the extension of the minimum cost flow algorithm for phase unwrapping of multitemporal differential SAR interferograms. *Ieee Trans. Geosci. Remote Sens.* **2006**, *44*, 2374–2383. [CrossRef]
52. Shi, M.; Peng, J.; Chen, X.; Zheng, Y.; Yang, H.; Su, Y.; Wang, G.; Wang, W. An Improved Method for InSAR Atmospheric Phase Correction in Mountainous Areas. *IEEE J. Sel. Top. Appl. Earth Obs. Remote Sens.* **2021**, *14*, 10509–10519. [CrossRef]
53. Hu, X.; Wang, T.; Pierson, T.C.; Lu, Z.; Kim, J.; Cecere, T.H. Detecting seasonal landslide movement within the Cascade landslide complex (Washington) using time-series SAR imagery. *Remote Sens. Environ.* **2016**, *187*, 49–61. [CrossRef]
54. Notti, D.; Meisina, C.; Zucca, F.; Colombo, A. Models to predict Persistent Scatterers data distribution and their capacity to register movement along the slope. In Proceedings of the Fringe 2011 Workshop, Frascati, Italy, 19–23 September 2011; pp. 19–23.
55. Notti, D.; Herrera, G.; Bianchini, S.; Meisina, C.; García-Davalillo, J.C.; Zucca, F. A methodology for improving landslide PSI data analysis. *Int. J. Remote Sens.* **2014**, *35*, 2186–2214. [CrossRef]
56. Plank, S.; Singer, J.; Minet, C.; Thuro, K. Pre-survey suitability evaluation of the differential synthetic aperture radar interferometry method for landslide monitoring. *Int. J. Remote Sens.* **2012**, *33*, 6623–6637. [CrossRef]
57. Li, M.H.; Zhang, L.; Yang, M.S.; Liao, M.S. Complex surface displacements of the Nanyu landslide in Zhouqu, China revealed by multi-platform InSAR observations. *Eng. Geol.* **2023**, *317*, 107069. [CrossRef]
58. van Natijne, A.L.; Bogaard, T.A.; van Leijen, F.J.; Hanssen, R.F.; Lindenbergh, R.C. World-wide InSAR sensitivity index for landslide deformation tracking. *Int. J. Appl. Earth Obs. Geoinf.* **2022**, *111*, 102829. [CrossRef]
59. Song, C.; Yu, C.; Li, Z.H.; Pazzi, V.; Del Soldato, M.; Cruz, A.; Utili, S. Landslide geometry and activity in Villa de la Independencia (Bolivia) revealed by InSAR and seismic noise measurements. *Landslides* **2021**, *18*, 2721–2737. [CrossRef]
60. Sharifi, S.; Macciotta, R.; Hendry, M.; Rotheram-Clarke, D.; Huntley, D. Evaluating topography-based methods in 3D decomposition of InSAR 1D velocities obtained for translational landslides: Thompson River valley in Canada. *Landslides* **2023**, *21*, 411–427. [CrossRef]
61. Kang, Y.; Lu, Z.; Zhao, C.Y.; Qu, W. Inferring slip-surface geometry and volume of creeping landslides based on InSAR: A case study in Jinsha River basin. *Remote Sens. Environ.* **2023**, *294*, 113620. [CrossRef]
62. Zhu, Y.F.; Yao, X.; Yao, L.H.; Zhou, Z.K.; Ren, K.Y.; Li, L.J.; Yao, C.C.; Gu, Z.K. Identifying the Mechanism of Toppling Deformation by InSAR: A Case Study in Xiluodu Reservoir, Jinsha River. *Landslides* **2022**, *19*, 2311–2327. [CrossRef]
63. Grant, M.; Boyd, S.; Cvx, Y.Y. *Matlab Software for Disciplined Convex Programming*, version 1.0 beta 3; CVX Research, Inc.: Austin, TX, USA, 2006.
64. Krishna, K.; Narasimha Murty, M. Genetic K-means algorithm. *IEEE Trans. Syst. Man Cybern. Part B (Cybern.)* **1999**, *29*, 433–439. [CrossRef] [PubMed]
65. MV, S.; MN, G. A Modified BM3D Algorithm for SAR Image Despeckling. *Procedia Comput. Sci.* **2015**, *70*, 69–75. [CrossRef]
66. Huang, W.L.; DeVries, B.; Huang, C.Q.; Lang, M.W.; Jones, J.W.; Creed, I.F.; Carroll, M.L. Automated Extraction of Surface Water Extent from Sentinel-1 Data. *Remote Sens.* **2018**, *10*, 797. [CrossRef]